# Targeting FSP1 triggers ferroptosis in lung cancer

Katherine Wu[1,2*], Alec J Vaughan[1,2*], Jozef P Bossowski[1,3], Yuan Hao[1,3], Aikaterini Ziogou[1,3], Seon Min Kim[4], Tae Ha Kim[4], Mari N Nakamura[1,3], Ray Pillai[1,5,6], Mariana Mancini[1,3], Sahith Rajalingam[1,3], Mingqi Han[7,8], Toshitaka Nakamura[10], Lidong Wang[9], Suckwoo Chung[1,3], Diane Simeone[9], David Shackelford[7,8], Yun Pyo Kang[4], Marcus Conrad[10, 11], Thales Papagiannakopoulos[1,3#]

[1]Department of Pathology, New York University Grossman School of Medicine, New York, NY, USA.

[2]Vilcek Institute of Graduate Biomedical Sciences, New York University Grossman School of Medicine, New York, NY, USA.

[3]Laura and Isaac Perlmutter Cancer Center, New York University Langone Health, New York, NY, USA.

[4]College of Pharmacy and Research Institute of Pharmaceutical Sciences, Seoul National University, Seoul, Korea

[5]Division of Pulmonary and Critical Care Medicine, Department of Medicine, VA New York Harbor Healthcare System, New York, USA.

[6]Division of Pulmonary, Critical Care, and Sleep Medicine, Department of Medicine, New York University Grossman School of Medicine, New York, USA.

[7]Pulmonary and Critical Care Medicine, David Geffen School of Medicine (DGSOM), University of California Los Angeles (UCLA), Los Angeles, CA, USA.

[8]Jonsson Comprehensive Cancer Center, UCLA, Los Angeles, CA, USA.

[9]Moores Cancer Center, University of California, San Diego, La Jolla, CA, USA

[10]Institute of Metabolism and Cell Death, Molecular Targets and Therapeutics Center, Helmholtz Munich, Neuherberg, Germany.

[11]Translational Redox Biology, Technical University of Munich (TUM), TUM Natural School of Sciences, Garching, Germany.

*These authors contributed equally

#Correspondence to:

Thales Papagiannakopoulos, PhD, thales.papagiannakopoulos@nyulangone.org

Key words: lung cancer, ferroptosis, FSP1, GPX4

**ABSTRACT**

Pre-clinical and clinical studies have demonstrated how dietary antioxidants or mutations activating antioxidant metabolism promote cancer, highlighting a central role oxidative stress in tumorigenesis. However, it is unclear if oxidative stress ultimately increases to a point of cell death. Emerging evidence indicates that cancer cells are susceptible to ferroptosis, a form of cell death that is triggered by uncontrolled lipid peroxidation. Despite broad enthusiasm about harnessing ferroptosis as a novel anti-cancer strategy, it remains unknown whether ferroptosis is a barrier to tumorigenesis and if it can be leveraged therapeutically. Using genetically-engineered mouse models (GEMMs) of lung adenocarcinoma (LUAD), we performed tumor specific loss-of-function studies of the two key ferroptosis suppressors, *glutathione peroxidase 4* (*Gpx4*) and *ferroptosis suppressor protein 1* (*Fsp1*), and observed increased lipid peroxidation, ferroptosis and robust suppression of tumorigenesis, suggesting that lung tumors are highly sensitive to ferroptosis. Furthermore, across multiple pre-clinical models, we found that FSP1 was selectively required for ferroptosis protection *in vivo*, but not *in vitro*, underscoring a heightened need to buffer lipid peroxidation under physiological conditions. Lipidomic analyses revealed that Fsp1-knockout ($Fsp1^{KO}$) tumors had an accumulation of lipid peroxides, and inhibition of ferroptosis with genetic, dietary, or pharmacological approaches effectively restored the growth of $Fsp1^{KO}$ tumors *in vivo*. Unlike *GPX4*, *FSP1* expression was prognostic for disease progression and poorer survival in LUAD patients, highlighting its potential as a viable therapeutic target. Moreover, given the critical role of GPX4 in multiple tissues, there is a greater therapeutic window for targeting FSP1. To this end, we demonstrated that pharmacologic inhibition of FSP1 had significant therapeutic benefit in pre-clinical lung cancer models. Our studies highlight the importance of ferroptosis suppression *in vivo* and pave the way for FSP1 inhibition as a therapeutic

53 strategy to improve disease outcome in lung cancer patients.

54

55 **MAIN TEXT**

56 Ferroptosis is a non-apoptotic, oxidative stress-dependent mechanism of cell death that is
57 uniquely distinguished by lipid peroxidation of polyunsaturated fatty acids of membrane
58 phospholipids (PUFA-PL)[1,2]. Lipid peroxidation involves the formation of lipid and lipid peroxyl
59 radicals which, in auto-oxidative propagation reactions, generate lipid hydroperoxides. Aberrant,
60 unrestricted lipid peroxidation results in altered membrane integrity, cell swelling, and ultimately
61 membrane rupture[3,4]. In recent years, growing interest in ferroptosis has elucidated key
62 mechanisms of lipid peroxidation regulation. Cells depend on several enzymes to protect against
63 ferroptosis[5-11], of which Glutathione Peroxidase 4 (GPX4) and Ferroptosis Suppressor Protein 1
64 (FSP1) are the most notable. GPX4 catalyzes the reduction of PUFA-PL hydroperoxides to non-
65 toxic alcohols. FSP1 catalyzes the reduction of extramitochondrial Coenzyme $Q_{10}$ (CoQ), a highly
66 potent lipid radical-trapping antioxidant (RTA). On the other hand, cells can be sensitized to
67 ferroptosis through PUFA-PL composition[12] and biosynthesis by Long-chain Acyl-CoA Synthase
68 4 (ACSL4)[13-15]. Apart from these cellular pathways, exogenous lipid RTAs, such as liproxstatin-1
69 (LIP1), ferrostatin-1 (FER1), Vitamin E (VitE), and Vitamin K (VitK), have also been shown to
70 specifically inhibit ferroptosis[1,6,16-18].

71 Emerging evidence indicates that cancer cells, including drug-resistant cells that have
72 adopted a mesenchymal state[19,20], are highly sensitive to lipid peroxidation *in vitro*, garnering
73 excitement about harnessing ferroptosis as a novel anti-cancer strategy. Though there have been
74 extensive studies characterizing GPX4 and more recently FSP1 in various diseases[21,22], whether
75 ferroptosis constitutes a barrier to tumorigenesis and the functional roles of GPX4 and FSP1 in *in*

76 *vivo* cancer models remain poorly characterized. To date, FSP1 has been shown to be a critical
77 ferroptosis suppressor only in the absence of GPX4[7,8,23]. However, given the high toxicity, poor
78 selectivity, and low to limited bioavailability of GPX4 inhibitors *in vivo*[24,25] as well as the only
79 recent development of FSP1 inhibitors, the majority of which do not have *in vivo* efficacy[7,23,26-29],
80 much work remains to demonstrate that ferroptosis induction could indeed be a therapeutic strategy
81 for cancer[30].

82 Here we show that genetic knockout of either Gpx4 or Fsp1 in genetically-engineered
83 mouse models (GEMMs) of autochthonous Kras-driven lung adenocarcinoma (LUAD)[31-35] results
84 in dramatic restriction of lung tumorigenesis. We demonstrate that disruption of Fsp1, often
85 considered a backup axis of ferroptosis suppression, is unexpectedly sufficient to trigger exhibit
86 enhanced lipid peroxidation in lung tumors. We confirm that Fsp1 deletion across several human
87 cancer cell lines with various oncogenic drivers, co-mutations, and tissue lineages consistently
88 lead to *in vivo* tumor restriction. As ferroptosis can be functionally defined as a modality of cell
89 death resulting from elevated lipid peroxides and rescued only with inhibitors of lipid peroxidation,
90 we further demonstrate that Fsp1-knockout ($Fsp1^{KO}$) tumors have increased oxidized PUFA-PLs
91 and that administration of lipid RTAs, as well as genetic loss of Acsl4, effectively restores lung
92 tumorigenesis. Finally, we report that FSP1 is upregulated as LUAD tumors progress and show
93 that FSP1 inhibition suppresses tumor growth and prolongs survival in multiple pre-clinical cancer
94 models. Given the prevalence and mortality rates of *KRAS*-mutant LUAD, as well as the lack of
95 tractable pre-clinical models to effectively investigate tumor ferroptosis, our work utilizes novel
96 *in vivo* models to characterize and harness ferroptosis induction, particularly via FSP1
97 perturbation, as a therapeutic approach for lung cancer.
98

99 **Lung tumors require Gpx4 to prevent ferroptosis**

100 GPX4 is considered the primary mediator of ferroptosis suppression that has been shown
101 to be essential across a plethora of murine and human cancer cells[5,25,36,37]. Therefore, we sought to
102 interrogate whether GPX4, and more broadly ferroptosis suppression, is a requirement for lung
103 tumorigenesis *in vivo*. Using a well-established GEMM of LUAD (*Kras*$^{LSL\text{-}G12D/+}$, *Tp53*$^{fl/fl}$,
104 *Rosa26*$^{LSL\text{-}Cas9/LSL\text{-}Cas9}$), we initiated Kras$^{G12D/+}$, Tp53$^{-/-}$ (KP) tumors by intratracheal delivery of
105 lentiviruses expressing CRE-recombinase and dual sgRNAs[38] against either Gpx4 (sg*Gpx4*) or
106 non-targeting control (sg*Neo*), enabling CRISPR/Cas9-mediated Gpx4-knockout (Gpx4$^{KO}$) or
107 wildtype (WT) control tumors, respectively. Concurrently, we treated a cohort of animals with
108 each tumor genotype with Liproxstatin-1 (LIP1), a potent lipid RTA and ferroptosis inhibitor,
109 throughout the entire course of tumorigenic progression (Fig. 1a). Tumor-specific Gpx4 deletion
110 (sg*Gpx4*) led to a significant decrease in lung tumor burden that was not observed in sg*Gpx4*
111 tumor-bearing mice treated with LIP1 (Fig. 1b-d). Efficient Gpx4 deletion was verified by
112 immunohistochemistry (IHC), with less than 15% of tumors in the in sg*Gpx4* group still staining
113 positive for Gpx4 (Extended Data Fig. 1a). IHC for 4-hydroxy-2-noneal (4-HNE), a marker for
114 lipid peroxidation in tissues (Extended Data Fig. 1b)[16], revealed significantly higher levels of lipid
115 peroxidation in sg*Gpx4* tumors compared to control sg*Neo* lung tumors, which was blunted with
116 LIP1 treatment (Fig. 1e, f).

117 Similar to our *in vivo* observations, CRISPR/Cas9-mediated Gpx4$^{KO}$ in KP LUAD cells
118 resulted in a near complete loss of viability and clonogenicity that was fully rescued by the addition
119 of LIP1 (Extended Data Fig. 1c). Targeted lipidomics to profile oxidized phosphatidylcholine
120 (PCs) and phosphatidylethanolamine (PEs) species in KP LUAD cells treated with RSL3, a
121 covalent Gpx4 inhibitor and ferroptosis inducer, revealed a higher abundance of oxidized

122 phospholipids in RSL3-treated cells that again was decreased in cells treated with concomitant
123 LIP1 (Extended Data Fig. 1d). On the other hand, Gpx4 overexpression ($Gpx4^{OE}$) in KP LUAD
124 cells had no impact on cell viability or clonogenicity basally (Extended Data Fig. 1e) but did confer
125 greater resistance to ferroptosis *in vitro* (Extended Data Fig. 1f). Similarly, supplementation of KP
126 LUAD cells with sodium selenite ($Na_2SeO_3$) to increase translation of Gpx4[39], a selenoprotein,
127 resulted in a corresponding boost in Gpx4 expression and enhanced ferroptosis resistance *in vitro*
128 (Extended Data Fig. 1g). Taken together, these results demonstrate that Gpx4 is essential for lung
129 tumors to evade ferroptosis and provide evidence that ferroptosis induction may be an effective
130 anti-cancer strategy.
131
132 **Unlike GPX4, FSP1 is upregulated in LUAD and prognostic of outcome**
133 Given our observation that Gpx4 was required for lung tumorigenesis in a GEMM that
134 closely recapitulates human LUAD development and progression, we next asked whether there
135 was clinical evidence suggesting that ferroptosis regulators in general are altered in lung cancer[40].
136 Although GPX4 expression was modestly increased in *KRAS*-mutant LUAD tumors compared to
137 normal lung tissue, there was no correlation with patient tumor stage or overall patient survival
138 (Extended Data Fig. 1h, i). Concordantly, Gpx4 protein levels also did not change during
139 autochthonous LUAD progression in KP GEMM tumors (Extended Data Fig. 1j).
140 Since GPX4 expression did not appear to correlate with any clinical prognostic factors in
141 *KRAS*-mutant LUAD patients, we next investigated FSP1, a second axis of ferroptosis surveillance
142 (Fig. 2a). We found that FSP1 expression was robustly increased in *KRAS*-mutant LUAD patient
143 tumors compared to normal lung and exhibited a positive correlative trend with higher tumor
144 stages (Extended Data Fig. 2a). Additionally, high FSP1 expression correlated with poor survival

145 in *KRAS*-mutant LUAD patients (Fig. 2b). Unlike Gpx4, Fsp1 protein levels increased temporally
146 as lung tumors progressed from adenomas to adenocarcinomas in KP GEMMs (Figs. 2c, d).
147 Altogether, these findings suggest that FSP1 may constitute a major suppressor of ferroptosis in
148 LUAD and is potentially a more viable therapeutic target than GPX4 for lung cancer patients.

149 Since prior studies have suggested that FSP1 may be regulated by KRAS signaling[41] to
150 further determine whether FSP1 upregulation was specific to *KRAS*-mutant LUAD, we stratified
151 LUAD patients by major oncogenic mutations. Again, *FSP1* was robustly increased in tumors
152 relative to normal lung, and this upregulation was observed irrespective of driver mutation or
153 *KRAS* variant (Extended Data Fig. 2b, c). Although *FSP1* expression was more robustly
154 upregulated in *KRAS*-mutant tumors compared to *EGFR*-mutant tumors, LUAD tumors with
155 neither mutation also exhibited upregulation of *FSP1* to the same extent as *KRAS*-mutant tumors.
156 Next, we investigated whether MAPK/ERK pathway regulates FSP1 expression. Both *in vitro*
157 pathway inhibition with RMC-042, a pan-RAS inhibitor, in a panel of *KRAS*-mutant LUAD cell
158 lines as well as multi-immunofluorescence (IF) for co-expression of Fsp1 and pErk in KP GEMM
159 tumors revealed a lack of correlation between FSP1 expression and ERK activation (Extended
160 Data Fig. 2d, e). Thus, these data indicate that *FSP1* expression, at least in the context of LUAD,
161 may not be exclusively dependent on KRAS-mediated oncogenic signaling.

162 Given that patients with *KRAS*-mutant LUAD tumors often have concomitant mutations in
163 *STK11* and *KEAP1*, which portend more advanced disease and poorer prognosis[34,43], we also
164 wondered whether *FSP1* expression was impacted by these mutations. We observed that *FSP1*
165 was significantly increased in LUAD tumors with co-mutation of either *STK11* or *KEAP1*
166 (Extended Data Fig. 2f). Additionally, treatment of a panel of human LUAD cell lines with an
167 NRF2 activator, KI696, led to significantly increased *FSP1* gene expression (Extended Data Fig.

168 2g). Of note, these findings are in accordance with recent studies describing a role for NRF2, which
169 is activated by *KEAP1* mutations, in FSP1 upregulation[42].
170
171 **Fsp1 is required for lung tumorigenesis**
172 To systematically investigate the functional role of Fsp1 in lung cancer, we initiated
173 autochthonous KP LUAD tumors, this time with tumor-specific CRISPR/Cas9-mediated deletion
174 of either Fsp1 or Gpx4 (Fig. 2e). Strikingly, we found that genetic deletion of Fsp1 (sg*Fsp1*) in
175 KP LUAD tumors strongly suppressed lung tumorigenesis, resulting in significantly decreased
176 tumor burden to the same extent as Gpx4$^{KO}$ (sg*Gpx4*) tumors (Fig. 2f, g). Efficient Fsp1 deletion
177 was verified by immunohistochemistry (IHC), with less than 5% of tumors in the in sg*Fsp1* group
178 still staining positive for Fsp1 (Extended Data Fig. 3a). We did not observe significant changes to
179 the total number or size of tumors formed across the three biological groups (Extended Data Fig.
180 3b, c), which suggested that loss of Fsp1 or Gpx4 primarily impacts tumor progression rather than
181 tumor initiation. We also observed that Fsp1 or Gpx4 deletion resulted in higher proportions of
182 adenomas to adenocarcinomas compared to control tumors (Fig. 2h), indicating that Fsp1 and
183 Gpx4 are functionally important for malignant disease progression. Additionally, there were no
184 notable changes to tumor cell proliferation or apoptotic cell death (Extended Data Figs. 3d, e) in
185 sg*Fsp1* or sg*Gpx4* tumors. In contrast, TUNEL staining of Fsp1$^{KO}$ and Fsp1$^{WT}$ tumors revealed
186 increased cell death upon Fsp1 loss (Fig. 3l), which suggests that the decreased lung tumor burden
187 with Fsp1 or Gpx4 genetic deletion is likely due to increased tumor cell ferroptosis. Perhaps most
188 exciting though is the extent to which Fsp1 deletion phenocopied Gpx4 loss *in vivo*, as this
189 phenotype, to our knowledge, has not yet been reported in any other cell lines, tissues, or disease
190 models.

191

192 **Fsp1 is only essential for *in vivo* cancer cell growth**

193 The discovery of FSP1 as a key regulator of ferroptosis arose from genetic screens to
194 identify ferroptosis suppressors in the absence of functional GPX4[7,8]. Thus, FSP1 is generally
195 thought to control a secondary anti-ferroptotic axis whose function, at least *in vitro*, is masked
196 when GPX4 is intact. Accordingly, we observed that CRISPR/Cas9-mediated Fsp1 deletion in KP
197 LUAD cells had no impact on cell viability and clonogenicity *in vitro* (Fig. 2i, Extended Data Fig.
198 4a). As expected, Fsp1-knockout ($Fsp1^{KO}$) cells were more sensitive to RSL3 treatment than
199 isogenic Fsp1-wildtype ($Fsp1^{WT}$) cells and protected from RSL3-killing by LIP1 (Fig. 2j). Despite
200 the remarkable restriction of KP LUAD tumorigenesis by Fsp1 loss *in vivo*, our *in vitro* studies
201 indicated in contrast that Fsp1's anti-ferroptotic function was not required by KP LUAD cells in
202 the presence of Gpx4.

203 We sought to dissect this intriguing dichotomy and better understand the distinct *in vivo*
204 dependency of lung tumors on Fsp1. We first performed a series of syngeneic transplantation
205 experiments using isogenic KP, $Fsp1^{KO}$ and $Fsp1^{WT}$ cell lines with no proliferation differences *in*
206 *vitro* to systematically characterize the impact of Fsp1 loss on tumor growth and further interrogate
207 whether Fsp1-mediated tumor differences were specific to *in vivo* growth conditions (Fig. 2i,
208 Extended Fig. 4b). Consistently, we found that $Fsp1^{KO}$ cells formed significantly smaller tumors
209 in both immunocompetent subcutaneous xenografts (Extended Data Fig. 4c, d) as well as
210 orthotopic lung tumors (Fig. 2k, Extended Data Fig. 4e, f). Robust suppression of $Fsp1^{KO}$
211 orthotopic lung tumor growth was similarly observed in immunodeficient athymic (NU/J) mice
212 (Extended Data Fig. 4g), as well as in an immunogenic mouse model[43] (Extended Data Fig. 4h).
213 We also observed the same phenotype in age- and sex-matched Fsp1 wildtype versus Fsp1

214 knockout mice (Extended Data Fig. 4i). Collectively, these studies provide strong evidence that
215 Fsp1's pro-tumorigenic effect is primarily cell-intrinsic. Finally, Fsp1 overexpression ($Fsp1^{OE}$) in
216 KP LUAD cells exhibited no *in vitro* growth advantage (Extended Data Fig. 4j), had enhanced
217 resistance to RSL3-killing (Extended Data Fig. 4k), and accelerated growth of xenograft tumors
218 *in vivo* (Extended Data Fig. Fig. 4l, m). Altogether, these results suggest that Fsp1 is essential for
219 LUAD cells' survival *in vivo* and that increased Fsp1 expression is sufficient to promote *Kras*-
220 mutant tumorigenesis *in vivo*.
221
222 **FSP1 is required for the growth of multiple genetic subtypes of LUAD and pancreatic cancer**
223 To more thoroughly interrogate the functional importance of Fsp1 for tumorigenesis and
224 the translational potential for targeting Fsp1 in cancer, we assessed the requirement of FSP1 for
225 growth of xenograft tumors from human LUAD cell lines harboring a variety of driver mutations,
226 including *KRAS, NRAS, EGFR, TP53, STK11* and *KEAP1*. We found that CRISPR/Cas9-mediated
227 FSP1 genetic deletion consistently and markedly decreased tumor growth in all models tested.
228 Specifically, $Fsp1^{KO}$ (sg*FSP1*) in H2009 (*KRAS*, *TP53* mutant), H1299 (*NRAS*, *TP53* mutant), PC9
229 and H1975 (*EGFR, TP53* mutant) LUAD cells led to robust suppression of subcutaneous tumor
230 growth (Fig. 3a-d), but, analogous to aforementioned studies, did not impact proliferation or
231 viability of cells *in vitro*, unless treated with RSL3 (Extended Data Fig. 5a-d). To assess whether
232 *KRAS*-mutant tumors with *STK11* (LKB1) and/or *KEAP1* mutation also depend on FSP1, we
233 performed CRISPR/Cas9-mediated FSP1 deletion in A549 (*KRAS, KEAP1, STK11* mutant) and
234 16645 (*Kras* mutant, *Stk11*-null) LUAD cells. Again, we observed a dependency for FSP1 *in vivo*
235 (Fig. 3e, f) but not *in vitro* (Extended Data Figure 5e-f). Together these data provide further

236 evidence that FSP1 is indeed required for *in vivo* LUAD tumor growth irrespective of driver and
237 co-mutations.

238 Finally, we asked if Kras-driven tumors of a different lineage also exhibited a requirement
239 for Fsp1 *in vivo*. Excitingly, transplantation of pancreatic adenocarcinoma (PDAC) *Kras*, *Tp53*
240 mutant (KPC7) cells with CRISPR/Cas9-mediated Fsp1 deletion also led to a robust tumor
241 suppression *in vivo* (Fig. 3g, Extended Data Fig. 5g), mirroring the phenotype observed
242 consistently in LUAD models and suggesting that FSP1 dependency *in vivo* may extend to other
243 tissue lineages.

244

245 **Ferroptosis restriction restores Fsp1$^{KO}$ tumors**

246 We hypothesized that defective regulation of lipid peroxidation and subsequent induction
247 of ferroptosis was the mechanism underlying FSP1$^{KO}$ tumorigenic suppression. To assess this, we
248 first performed epilipidomic analysis of Fsp1$^{WT}$ and Fsp1$^{KO}$ orthotopic lung tumors and observed
249 that Fsp1$^{KO}$ tumors exhibited increased abundance of oxidized and truncated PC/PE species,
250 indicative of increased cellular lipid peroxidation (Fig. 4a). We then asked whether ectopic
251 overexpression of Fsp1 or Gpx4 (Extended Data Fig. 6a, b) was sufficient to restore the growth of
252 Gpx4 or Fsp1$^{KO}$ tumors, which would shed light about the capacity for each ferroptosis defense
253 arm to compensate for the loss of the other. Indeed, we found that Fsp1$^{OE}$ and Gpx4$^{OE}$ effectively
254 restored the growth of Gpx4$^{KO}$ and Fsp1$^{KO}$ tumors, respectively (Fig. 4b-c, Extended Data Fig. 6c,
255 d). These data implicated that tumors require extensive buffering capacity against lipid
256 peroxidation and that while Gpx4 and Fsp1 act through distinct pathways, each can compensate
257 for the loss of the other.

258 Mechanistically, Fsp1 has been shown to suppress ferroptosis by reducing CoQ, an

259 endogenous RTA, and this function is dependent on its localization to the plasma membrane. We
260 utilized a LC/MS-based, quantitative method to determine the abundance of CoQ in tumors, which
261 revealed that Fsp1$^{KO}$ tumors had a significantly decreased ratio of reduced $CoQ_9H_2$ to oxidized
262 $CoQ_9$ (Fig. 4d). This decreased ratio was not present in genotypically matched cells at baseline *in*
263 *vitro*, but interestingly upon treatment with RSL3, Fsp1$^{KO}$ cells mimicked the decreased
264 $CoQ_9H_2$/CoQ9 observed in tumors. Prior studies have described that mutation of the
265 myristoylation sequence that targets FSP1 to the plasma membrane renders FSP1 unable to protect
266 against lipid peroxidation *in vitro*[7,8], which we also observed in KP LUAD cells (Extended Data
267 Fig. 6e, f). We anticipated that expression of this mutant Fsp1 (Fsp1$^{mut}$) would be similarly unable
268 to restore Fsp1$^{KO}$ tumor growth. Indeed, while Fsp1$^{WT}$-restored tumors grew quickly, both Fsp1$^{mut}$
269 and Fsp1$^{KO}$ tumors had decreased growth (Extended Data Fig. 6g). Taken together, these data
270 suggest that tumors require Fsp1 enzymatic activity and subcellular localization *in vivo* to
271 specifically buffer against ferroptosis.

272 Next, we asked whether ferroptosis suppression, via several orthogonal approaches
273 including tumor-specific Acsl4 knockout (Acsl4$^{KO}$), dietary VitE supplementation, and LIP1
274 treatment would restore Fsp1$^{KO}$ tumor growth. Loss or inhibition of Acsl4, which limits PUFA-PL
275 supply and restricts lipid peroxidation (Fig. 4e), has previously been shown to be protective against
276 ferroptosis in Gpx4$^{KO}$ cells *in vitro*[13-15]. Therefore, we sought to determine whether genetic
277 deletion of Acsl4 would suppress ferroptosis and rescue the growth of Fsp1$^{KO}$ tumors *in vivo*. We
278 performed CRISPR/Cas9-mediated genetic deletion of Acsl4 (sg*Acsl4*) in isogenic KP, Fsp1$^{KO}$
279 and Fsp1$^{WT}$ cells. We observed that loss of Acsl4 did not impact cell viability but robustly rescued
280 RSL3-induced ferroptosis *in vitro*, in both Fsp1$^{WT}$ and Fsp1$^{KO}$ cells (Extended Data Fig. 6h).
281 Importantly, Acsl4 deletion significantly restored Fsp1$^{KO}$ lung tumor growth *in vivo* (Extended

282 Data Fig. 6i) and mice with Acsl4, Fsp1-double knockout tumors were found to have increased
283 endpoint disease burden (Fig. 4f, Extended Data Figure 6j) and decreased overall survival
284 (Extended Data Fig. 6k). Furthermore, tumor-specific Acsl4$^{KO}$ led to a basal acceleration of tumor
285 growth (Extended Data Fig. 6i) and decreased overall survival (Extended Fig. 6k), suggesting that
286 decreased accumulation of PUFA-PL in lung tumors may also protect against ferroptosis *in vivo*.

287 VitE is nature's premier lipophilic antioxidant and is specifically able to scavenge lipid
288 radicals and protect against ferroptosis (Fig. 4e). Therefore, we decided to test whether dietary
289 VitE supplementation could rescue the growth of Fsp1$^{KO}$ lung tumors. High versus low VitE diets
290 *ad libitum* was provided to animals either before or after tumor initiation (Fig. 4g), and we found
291 that increased dietary VitE accelerated Fsp1$^{KO}$ tumor growth (Fig. 4h, i), with no impact on growth
292 of Fsp1$^{WT}$ tumors (Extended Data Fig. 6l).

293 Lastly, since LIP1 suppressed tumor lipid peroxidation and entirely mitigated the impact
294 of Gpx4 loss on KP LUAD tumorigenesis (Fig. 1b-d), we conducted parallel studies to investigate
295 whether LIP1 also blunts ferroptosis in and restores Fsp1$^{KO}$ tumorigenesis. In the orthotopic lung
296 tumor model, we observed a tendency for Fsp1$^{KO}$ tumors to grow more quickly with daily LIP1
297 administration (Extended Data Fig. 6m). In the KP LUAD GEMM (Extended Data Fig. 6n), which
298 was conducted in accordance with experimental parameters for Gpx4$^{KO}$ GEMM studies, LIP1
299 treatment significantly increased autochthonous Fsp1$^{KO}$ (sg*Fsp1*) tumor burden (Extended Data
300 Fig. 6o). Moreover, sg*Fsp1* tumors stained positively for 4-HNE, which was effectively
301 suppressed by LIP1 treatment (Extended Data Fig. 6p). As observed with VitE supplementation,
302 timing of LIP1 treatment did not appear to have a differential impact, as LIP1 treatment after
303 tumors were already established was equally effective at restoring sg*Fsp1* lung tumorigenesis (Fig
304 4j-l). Altogether, these studies provide clear evidence that LUAD tumors require Fsp1 to protect

305 against ferroptosis *in vivo* and suggest that increased lipid peroxidation is a barrier for tumor
306 growth and progression.
307
308 **Pharmacologic inhibition of FSP1 promotes ferroptosis and suppresses tumor growth**
309 With the growing interest in harnessing ferroptosis to kill tumor cells, several FSP1
310 inhibitors have been developed[7,27], though the majority are effective only *in vitro* against human
311 FSP1 (hFSP1) in the context of Gpx4 loss or inhibition (Extended Data Fig. 7a-d). Recently,
312 icFSP1 was developed as the first human FSP1 (hFSP1) inhibitor with *in vivo* stability and
313 efficacy, albeit solely in tumors with concomitant Gpx4 loss[23]. Accordingly, we also saw that
314 icFSP1 treatment *in vitro* did not impact cell viability (Extended Data Fig. 7e) unless RSL3 was
315 added (Extended Data Fig. 7f). Given that murine and human FSP1 are highly conserved in
316 sequence and structure, we generated a hybrid tumor model in which hFSP1 was expressed in
317 murine KP, $Fsp1^{KO}$ tumors. We observed that expression of either murine or human FSP1 resulted
318 in similar acceleration of tumor growth compared to $Fsp1^{KO}$ tumors (Extended Data Fig. 7g, h),
319 which indicated that hFSP1 can functionally compensate for mFsp1 *in vivo*.
320 Using this hybrid tumor model, we next tested whether icFSP1 had therapeutic benefit
321 against lung cancer. Excitingly, we found that FSP1 inhibition as a monotherapy improved overall
322 survival of lung tumor-bearing mice, nearly to the extent of genetic Fsp1 deletion (Fig. 5a). To
323 determine whether the therapeutic effect of icFSP1 was indeed due to the induction of ferroptosis,
324 we asked whether LIP1, which we expected to inhibit lipid peroxidation induced by FSP1
325 inhibition, rescued tumor suppression in icFSP1-treated animals. In correlation with the survival
326 data, we observed that icFSP1-treatment significantly decreased tumor growth when compared to
327 vehicle treated animals, and importantly, concomitant LIP1 treatment abrogated the tumor-

328 suppressive effect of icFSP1 treatment (Fig. 5b, Extended Data Fig. 7c). Further, to test whether
329 icFSP1 was exerting an on-target, tumor-specific effect, we repeated the treatment study with an
330 internal control— lung tumors expressing $FSP1^{Q319K}$, a mutant that is resistant to icFSP1 but
331 maintains anti-ferroptotic function (Extended Data Fig. 7a, b). We found that icFSP1 treatment
332 specifically extended overall survival of mice bearing tumors with $hFSP1^{WT}$ but not $hFSP1^{Q319K}$
333 (Fig. 5c), indicating that indeed the tumor suppression seen with icFSP1 treatment was due to
334 inhibitor activity directly on tumor cells.

335 We wondered whether icFSP1 treatment also impacted the tumor microenvironment
336 (TME), but we found no differences in the proportion of total T cells, neutrophils, alveolar, or
337 interstitial macrophages between the treatment groups (Extended Data Fig. 7j). These data further
338 suggest that icFSP1 primarily exerts on-target, tumor-specific effects, though more granular
339 immune profiling is needed to determine the potential impact, and thus potential side effects, of
340 FSP1 inhibition on TME. Finally, we utilized a PDX model (LX465; *KRAS*$^{G12D}$, *TP53*-mutant) to
341 further assess the therapeutic potential of FSP1 inhibition. Excitingly, we found that icFSP1
342 treatment significantly decreased PDX tumor growth (Fig. 5d), further bolstering the translational
343 potential of targeting FSP1 in LUAD patients. These pre-clinical studies with icFSP1 are the first
344 to demonstrate that FSP1 is a promising therapeutic target, and our work highlight FSP1 inhibition
345 as a novel therapeutic strategy to improve disease outcome in lung cancer patients.

346

347 **DISCUSSION**

348 Cancer is a disease of hyperproliferation, and cancer cells increase their metabolic output
349 to support sustained growth. This occurs at the cost of increased ROS production that can damage
350 macromolecules, such as lipids, and have deleterious effects[44,45]. One such effect is excessive lipid

351 peroxidation of membrane-associated PUFA-PLs, which can lead to ferroptosis, a unique non-
352 apoptotic mechanism of cell death. Through our systematic interrogation of the key mechanisms
353 that regulate aberrant lipid peroxidation *in vivo*, we demonstrated that ferroptosis constitutes a
354 barrier to lung cancer and that lung tumors rely on Gpx4 and uniquely, Fsp1 to overcome
355 ferroptosis and sustain tumorigenesis (Extended Data Fig. 7k, l).

356 Our work specifically highlights the dependence of lung tumors on Fsp1 *in vivo*, even in
357 the presence of functional Gpx4 (Extended Data Fig. 7k). This is the first report of a context where
358 Fsp1 and Gpx4 are independently required for ferroptosis suppression and therefore either can
359 impact disease outcome. Moreover, analysis of GEMM and human lung tumors demonstrated that
360 FSP1 levels increase during tumor progression and correlate with poor survival. In contrast, GPX4
361 levels are ubiquitous in tumors and most tissues. Given that germline $Gpx4^{KO}$ mice are not viable[46],
362 whereas $Fsp1^{KO}$ mice are with no notable physiological defects[16,47,48], the therapeutic window for
363 targeting FSP1 with fewer toxic side effects is expected to be much greater than for GPX4.
364 Furthermore, loss of GPX4 is toxic to T cells which would suppress any anti-tumor immune
365 responses[49,50]. Leveraging this unique requirement for Fsp1 in lung cancer, our studies demonstrate
366 the therapeutic benefit of FSP1 inhibition in promoting ferroptosis and suppressing tumor growth
367 and extending survival as a monotherapy in aggressive pre-clinical lung cancer models. Our
368 studies underscore the value of *in vivo* pre-clinical models in capturing physiologically relevant
369 metabolic dependencies that may be missed *in vitro*, and pave the way for developing FSP1
370 inhibitors for clinical testing in lung cancer patients.

371

372

373

374 **Methods**

375 *Cell lines*

376 KP LUAD cell lines were obtained from the laboratory of Tyler Jacks. KP, Fsp1$^{KO}$ cell lines were
377 generated by transient transfection of PX458 (Addgene #48138) expressing an sgRNA targeting
378 Fsp1. Single GFP positive clones were selected and Fsp1 loss was validated by western blot. All
379 cell lines were maintained in DMEM or RPMI 160 (Corning) supplemented with 10% FBS (Sigma
380 Aldrich) and gentamicin (Invitrogen) and were tested for mycoplasma regularly (PlasmoTest,
381 InvivoGen). Genetic manipulation of cell lines was performed via lentiviral transduction of
382 plasmids, detailed in next section, followed by either puromycin (7ug/mL) or hygromycin
383 (800ug/mL) selection for 1 week.

384

385 *Cloning/lentivirus generation*

386 CRISPR/Cas9-mediated knockout of target genes was achieved by cloning sgRNAs into pLenti-
387 USEC or lentiCRISPRv2-puro vectors, as previously described[31]. In short, backbones were
388 digested with Esp3I (New England Biosciences) and purified with a gel extraction kit (QIAGEN).
389 sgRNAs were designed using CRISPick (Broad Institute), obtained from Integrated DNA
390 Technologies (Coralville, IA), annealed, phosphorylated, Esp3I-digested, and ligated into the
391 purified digested backbones using Quick Ligase (New England Biosciences). Double sgRNA
392 ultramers were designed and generated as previously described[38]. Briefly, ultramers were Gibson
393 assembled to digested pDonor_sU6 (Addgene #69351), Esp3I-digested, and ligated to purified
394 digested backbones. Gpx4, mFsp1, and hFSP1 expression plasmids were generated using Gibson
395 assembly of the respective cDNA into pLenti-v2-filler.

396 Lentivirus was generated by co-transfection of HEK293 cells with a viral vector and packaging

397 plasmids psPAX2 (Addgene #12260) and pMD2.G (Addgene #12259) using PEI transfection
398 reagent. Cell supernatant containing lentivirus was collected 72 hours after transfection and
399 filtered through 0.45 μM PVDF filters. For *in vivo* experiments, lentivirus was concentrated by
400 ultracentrifugation at 25,000rpm for 2 hours at 4°C. The viral pellet was resuspended in PBS and
401 stored at -80°C until use. Viral titer was quantified with the use of a Cre-dependent GreenGo
402 reporter cell line. For *in vitro* experiments, media containing virus was collected, filtered, and
403 added directly to recipient cells with polybrene at 8 μg/mL for 48 hours before selection.
404
405 *Mouse models*
406 All mouse experiments described in this study were approved by the NYU Institutional Animal
407 Care and Use Committee (IACUC). Animals were housed according to IACUC guidelines in
408 ventilated caging in a specific pathogen free animal facility. For all mouse studies, ≥ 4 mice were
409 used for each experimental condition. *Kras*$^{LSL\text{-}G12D/+}$; *Tp53*$^{fl/fl}$; *Rosa26*$^{LSL\text{-}Cas9/LSL\text{-}Cas9}$ (KPC
410 GEMMs) were bred as previously described[31-35]. C57BL/6J (JAX strain #000664) mice with the
411 appropriate genotype, aged 8 to 12 weeks were randomly selected to begin tumor initiation studies
412 with pUSEC lentivirus. Care was taken to ensure each experimental arm had an equal number of
413 male and female mice. Mice were intratracheally infected with lentiviruses as described and
414 monitored until experimental endpoint. Tumor burden was quantified by hematoxylin and eosin
415 (H&E) staining and analyzed using QuPath software as a measurement of total tumor area/total
416 lung lobe area. All quantifications were done with investigator blinded to the respective sample
417 genotypes. All transplantation experiments were performed using nude (JAX strain #002019),
418 NOD SCID Gamma (NSG; JAX strain #005557F), C57BL/6J Fsp1 KO (Conrad group[16]) or
419 C57BL/6J (JAX strain #000664) mice. For murine cell xenograft experiments, 100,000 cells in

420 100µl of phosphate-buffered saline (PBS) were injected subcutaneously into each flank of the
421 mouse. For the xenograft studies in Figure 3 the number of cells injected per flank and whether
422 they were injected with 50:50 PBS and Matrigel (Corning) are indicated in the following list:
423 H2009 (2 million cells +Matrigel), H1299 (1 million cells), PC9 (1 million cells), H1975 (2 million
424 cells +Matrigel), A549 (1 million cells), 16645 (500,000 cells), KPC7 (250,000 cells). For the
425 PDX experiment, tumors were implanted subcutaneously in NSG mice as previously described[34].
426 Tumors were measured by caliper, and volume was calculated based on 0.5 x length x width$^2$. For
427 orthotopic lung tumor experiments, 100,000 luciferase-expressing cells in 200µl of PBS were
428 injected intravenously into tail vein of mice. Tumor growth was measured by bioluminescence
429 (PerkinElmer IVIS Spectrum In Vivo Imaging System; D-luciferin, PerkinElmer #122799). Data
430 were analyzed using Living Image software.
431
432 *Antioxidant/drug treatments*
433 For LIP1 treatment, mice were dosed with 10 mg/kg Liproxstatin-1 (BOC Sciences) or Vehicle
434 (2% DMSO + 40%PEG300 + 2%Tween80 in sterile $H_2O$) by intraperitoneal injection for length
435 of time indicated in figure schematics. For icFSP1 treatment, mice were dosed with 50mg/kg
436 icFSP1 (WuXi LabNetwork) or vehicle (45% PEG300 in sterile PBS) by intraperitoneal injection
437 twice daily. High (TD.2108412) and low (TD.210841) irradiated Vitamin E diets were obtained
438 from Inotivco and provided *ad libitum* for length of time indicated in figure legends.
439
440 *Cell clonogenic and viability assays*
441 Cell clonogenic assays were conducted by seeding 2000 cells per well into 12-well dishes
442 (BD/Falcon) in RPMI-1640 media. After 12-16hrs, media containing RSL3 and/or LIP1 were

443 added to wells. After 5 days of growth, plates were washed twice with PBS and stained with 0.5%
444 crystal violet (Fisher Scientific) solution in 20% methanol. Plates were dried, scanned, and crystal
445 violet was quantified by solubilization with 10% acetic acid and measurement of absorbance at
446 592nm by spectrometer (Molecular Devices). Cell viability assays were conducted by seeding
447 2000 cells per well into white-walled, clear-bottom, 96-well plates (Corning) in RPMI-1640
448 media. After 12-16hrs, media containing RSL3, LIP1, and/or FSEN1, iFSP1, or icFSP1 were
449 added. After 3 days, cell viability was assessed by CellTiter-Glo (Promega) and luminescence was
450 measured by spectrometer (Molecular Devices).
451
452 *Immunoblotting*
453 Cells were plated to 75% confluency in a 6-well dish, and the following day cells were lysed on
454 ice with Pierce RIPA buffer (ThermoScientific) containing 1x protease/phosphatase inhibitor
455 cocktail (Thermo Fisher Scientific). Samples were sonicated in cooled 4°C water (12 rounds, 30
456 seconds on and 30 seconds off) and then centrifuged at 14000 rpm at 4°C for 15 minutes. The
457 supernatant was collected, and protein was quantified using the DC Rad Protein Assay kit. Protein
458 was diluted to 1 ug/uL with water and 4x NuPage LDS sample buffer, then boiled at 95°C for 10
459 minutes. 20 ug protein per well was loaded into Invitrogen 4-12% Bis-Tris gels and then
460 transferred onto PVDF membranes using a standard protocol. PVDF membranes were then
461 blocked using 5% BSA in TBST for 60 minutes at room temperature and incubated with primary
462 antibodies in 5% BSA overnight at 4°C. Primary antibodies were obtained as follows: Gpx4
463 (Abcam), Fsp1 (Proteintech), Acsl4 (Santa Cruz Biotechnologies), pERK (Cell Signaling), ERK
464 (Cell Signaling), and Hsp90 (BD Bioscences). The following day, membranes were washed in
465 TBST and incubated with HRP-conjugated secondary antibodies for 1 hour at room temperature.

466 Enhanced chemiluminescent horseradish peroxidase substrate (ThermoScientific SuperSignal
467 West PICO Plus) was added to the membrane for 1 minute, and the resulting membrane was
468 imaged using the General Electric Amersham Imager 680.
469
470 *Oxidized lipidomics*
471 For the Gpx4 KO experiment, cells were plated to 75% confluency in 6-well dish. The following
472 day, cells were treated with DMSO, RSL3 (0.5uM), or RSL3(0.5μM) + LIP1(100nM). After 8hrs,
473 cells were collected and washed in an antioxidant solution (PBS containing dibutylhydroxytoluene
474 (BHT; 100 μM) and diethylenetriamine pentaacetate (DTPA; 100 μM)) and centrifuged.
475 Supernatent was discarded and cell pellets were immediately frozen in liquid nitrogen and stored
476 at –80 °C. Frozen samples were sent on dry ice to Wayne State Lipidomics Core for metabolite
477 extraction and LC-MS analysis.
478 Fsp1 WT and KO tumor and cell lipidomic analysis were performed in the lab of Pyo Kang. Fsp1
479 WT and KO cells were plated at 75% confluency in 10 cm plates and treated as stated above. After
480 euthanasia, animals were perfused with the antioxidant solution (+3.8% trisodium citrate),
481 orthotopic tumors were microdissected, frozen in liquid nitrogen and stored at –80 °C. Mouse lung
482 cancer tissues were cryopulverized and extracted with chloroform:methanol (2:1, v/v) at a tissue
483 concentration of 25 mg $mL^{-1}$. For the cells, $1.0 \times 10^7$ cells were extracted by one milliliter of
484 chloroform:methanol (2:1, v/v). EquiSPLASH LIPIDOMIX® internal standard (Avanti Polar
485 Lipids) was added to the extraction solvent at 0.1 μg $mL^{-1}$ per lipid class. Samples were sonicated
486 on ice for 1 min using a VCX 130 probe sonicator (5 s on/off cycles), incubated for 30 min, and
487 centrifuged at 17,000 × g for 20 min at 4 °C. The supernatant was was dried under vacuum (EZ-2
488 Elite, Genevac), reconstituted in 10% of the original volume with isopropanol, and transferred to

489 glass autosampler vials for LC–MS analysis. Chromatographic separation was performed using a
490 Waters ACQUITY UPLC CSH C18 column (100 × 2.1 mm, 1.7 µm) with a VanGuard precolumn
491 (5 × 2.1 mm, 1.7 µm). Mobile phase A consisted of acetonitrile/water (60:40, v/v), and mobile
492 phase B of isopropanol/acetonitrile (90:10, v/v), both containing 5 mM ammonium formate and
493 0.1% formic acid. The column was maintained at 65 °C with a flow rate of 0.6 mL $min^{-1}$. The
494 gradient was as follows: 0–2 min, 15–30% B; 2–2.5 min, 30–48% B; 2.5–11 min, 48–82% B; 11–
495 11.5 min, 82–99% B; 11.5–12 min, 99% B; 12–12.1 min, 99–15% B; and 12.1–16 min, hold at
496 15% B for re-equilibration. Mass spectrometry was performed on a Q Exactive Plus Quadrupole-
497 Orbitrap (Thermo Fisher Scientific) equipped with a heated electrospray ionization (HESI) source
498 and operated in negative ion mode. Source settings were: sheath gas, 60 a.u.; auxiliary gas, 25 a.u.;
499 sweep gas, 2 a.u.; spray voltage, 3.0 kV; capillary temperature, 320 °C; S-lens RF level, 50%; and
500 auxiliary gas heater temperature, 370 °C. Parallel reaction monitoring (PRM) was carried out with
501 the following parameters: resolution, 17,500 at m/z 200; AGC target, $2 \times 10^5$; maximum injection
502 time, 50 ms; isolation window, m/z 1.2; and stepped normalized collision energies of 20, 30, and
503 40. The oxidized lipid analysis was adapted by previous PRM based analysis. [51] To generate the
504 PRM inclusion list, pooled sample extracts were first analyzed in DDA mode to identify the most
505 abundant polyunsaturated PC and PE species using Lipostar2.[52] These precursors were subjected
506 to in silico oxidation using LPPtiger2 to predict candidate oxidized lipids. A semi-targeted DDA
507 experiment was then conducted to confirm precursor detectability and finalize the inclusion list. [51]
508 Data were analyzed using Skyline (v24.1). [53] Quantification was based on fragment anions derived
509 from oxidized fatty acyl chains, with peak areas normalized to PC(15:0/18:1(d7)) or
510 PE(15:0/18:1(d7)) internal standards from the EquiSPLASH LIPIDOMIX® mixture.
511

512 *$CoQ_9$ and $CoQ_9H_2$ analysis*

513 $CoQ_9$ and $CoQ_9H_2$ analysis was conducted by modification of previous study [54]. The $D_9$-$CoQ_{10}$
514 standard was purchased from IsoSciences (Ambler, PA, USA). The $D_6$-$CoQ_{10}H_2$ standard was
515 synthesized from $D_6$-$CoQ_{10}$, which was obtained from Good Laboratory Practice Bioscience
516 (Montclair, CA, USA). The $CoQ_9$ standard was purchased from Tokyo Chemical Industry (Tokyo,
517 Japan), and $CoQ_9H_2$ was synthesized from $CoQ_9$. $D_6$-$CoQ_{10}H_2$ and $D_9$-$CoQ_{10}$ were used as internal
518 standards for the $CoQ_9H_2$ and $CoQ_9$, respectively. Chloroform: methanol (2:1, v/v), containing
519 internal standards of 0.5 μM of $D_6$-$CoQ_{10}H_2$ and $D_6$-$CoQ_{10}$ was used to extract mouse lung cancer
520 tissue at a tissue concentration of 25 mg $mL^{-1}$. For the cells, $1.0 \times 10^7$ cells were extracted by one
521 milliliter of same extraction solvent. Samples were then sonicated on ice for 1 min using a VCX
522 130 probe sonicator (5 s on/off cycles), incubated for 30 min, and centrifuged at 17,000 × g for
523 20 min at 4 °C. A 100 μL aliquot of the supernatant was transferred to glass autosampler vials for
524 LC–MS/MS analysis. The liquid chromatography conditions were identical to those used for
525 oxidized lipid analysis. Q Exactive Plus MS was operated in positive ion mode. Source settings
526 were as follows: sheath gas, 60 a.u.; auxiliary gas, 25 a.u.; sweep gas, 2 a.u.; spray voltage, 3.0 kV;
527 capillary temperature, 320 °C; S-lens RF level, 50%; and auxiliary gas heater temperature, 370 °C.
528 The mass range was m/z 120–1,200; resolution, 70,000 at m/z 200; AGC target, $1 \times 10^6$; and
529 maximum injection time, 100ms. By using EL–MAVEN (v0.12.0), the LC-MS peaks of $CoQ_9$,
530 $CoQ_9H_2$, $D_6$-$CoQ_{10}H_2$, $D_6$-$CoQ_{10}$, and $D_9$-$CoQ_{10}$ were identified by matching with standard library
531 and their peak areas were extracted with 10 ppm error range. Standard curves were generated using
532 known concentrations of $CoQ_9H_2$ and $CoQ_9$, and used to calculate the concentrations of $CoQ_9H_2$
533 and $CoQ_9$ in the samples fallowing an algorithm described in a previous study[54]

534
535

536 *Immunohistochemistry*

537 Tumor bearing mice were euthanized by carbon dioxide asphyxiation, after which the lungs were
538 dissected and fixed in 4% PFA solution overnight. Fixed lungs were washed with PBS 2x,
539 transferred, and stored in 70% ethanol, until cassette loading and paraffin embedding. Sections
540 were cut and stained with H&E. For immunohistochemistry with the exception of TUNEL
541 staining, sections were immunostained on a Leica BondRX automated stainer according to the
542 manufacturer's instructions. In brief, tissues underwent deparaffinization online, followed by
543 epitope retrieval for 20 minutes at 100º with Leica Biosystems ER2 solution (pH9, cat#AR9640),
544 endogenous peroxidase activity blocking with H2O2, and non-specific binding site blocking with
545 Rodent Block M (Biocare, cat# RBM961L) and Bond Primary Antibody Diluent (Leica
546 Biosystems, cat# AR9352). Sections were then incubated with primary antibodies against Gpx4
547 (Abcam), Fsp1 (courtesy of Dr. Marcus Conrad), 4-HNE (JaICA), Ki67, and Ccasp3 for 60
548 minutes at room temperature. Primary antibodies were detected with anti-rat HRP-conjugated
549 polymer (Biocare, cat# BRR4016H), 3,3'-diaminobenzidine (DAB) substrate (provided in the
550 Leica BOND Polymer Refine Detection System, cat# DS9800), and for 4-HNE staining Bond
551 DAB Enhancer (Leica Biosystems, cat# AR9432). Following counter-staining with hematoxylin,
552 slides were scanned at 40X on a Hamamatzu Nanozoomer (2.0HT). TUNEL staining was
553 performed by Histowiz Inc. (histowiz.com) according to their protocol.

554 For OPAL imaging, coronal 5 µm sections were immunostained on a Leica BondRx auto-stainer
555 according to the manufacturer's instructions. In brief, sections were deparaffiinized online and
556 then treated with 3% $H_2O_2$ to inhibit endogenous peroxidases, followed by antigen retrieval with
557 either ER1 (Leica, AR9961; pH6) or ER2 (Leica, AR9640; pH9) retrieval buffer at 100o for 20
558 minutes. After blocking with either Rodent Block M (Biocare, RBM961L) or Primary Antibody

559 Diluent (Leica, AR93520), slides were incubated with the first primary antibody (FSP1, courtesy
560 of Marcus Conrad, pERK1/2, CST, GPX4, Abcam) and secondary HRP polymer pair, followed
561 by HRP-mediated tyramide signal amplification with a specific Opal® fluorophore. Once the
562 Opal® fluorophore was covalently linked to the antigen, primary and secondary antibodies were
563 removed with a heat retrieval step. This sequence was repeated three more times with subsequent
564 primary and secondary antibody pairs, using a different Opal fluorophore with each primary
565 antibody (see table below for primary antibody sequence and reagent details). After antibody
566 staining, sections were counterstained with spectral DAPI (Akoya Biosciences, FP1490) and
567 mounted with ProLong Gold Antifade (ThermoFisher Scientific, P36935). Semi-automated image
568 acquisition was performed on an Akoya Vectra Polaris (PhenoImagerHT) multispectral imaging
569 system. Slides were scanned at 20X magnification using PhenoImagerHT 2.0 software in
570 conjunction with Phenochart 2.0 and InForm 3.0 to generate unmixed whole slide qptiff scans. All
571 image files were uploaded to the NYUGSoM's OMERO Plus image data management system
572 (Glencoe Software).
573
574 *Flow Cytometry*
575 Lung tissue was processed into a single cell suspension for flow cytometry as previously
576 described[41,53]. Briefly, prior to euthanasia, mice were injected with 2 ug of Anti-mouse CD45-
577 APC conjugated antibody (Biolegend, Clone 30-F11, 103111) retro-orbitally. Lungs were
578 harvested and digested with Collagenase (Sigma-Aldrich, C5138) and deoxyribonuclease I
579 (Sigma-Aldrich, DN25) followed by red blood cell lysis. Single cells were then resuspended in
580 FACS buffer and stained using antibodies listed in Table 1. Samples were run on the BD
581 LSRFortessa and analyzed on FlowJo version 10.

582

583 Table 1:

| Antigen | Fluorophore | Brand | Cat # | Clone |
|---|---|---|---|---|
| CD45 | PerCP/cy5.5 | Biolegend | 103132 | 30-F11 |
| CD11b | PE.CY7 | Biolegend | 101216 | M1/70 |
| CD11c | APC.Cy7 | Biolegend | 117324 | N418 |
| Ly6G | A700 | Biolegend | 127622 | 1A8 |
| MHCII | BUV737 | BD | 748708 | 2G9 |
| CD103 | BV605 | Biolegend | 121433 | clone 2E7 |
| CD64 | BV421 | Biolegend | 139309 | X54-5/7.1 |
| SiglecF | BV786 | BD | 740956 | E50-2440 |
| MertK | Biotin | R&D | BAF591 | AF591 |
| Secondary (Streptavidin) | BUV395 | BD | 564176 | - |
| CD45 | BUV737 | BD | 748371 | 30-F11 |
| CD3e | BV786 | BD | 740854 | eBio500A2 (500A2) |
| CD4 | Pacific blue | Invitrogen | MCD0428 | RM4-5 |
| CD8a | BV605 | EBioscience | 563152 | 53-6.7 |

584

585 *TCGA analyses*

586 Gene expression profiles of primary tumors and relevant clinical data of 515 LUAD patients were
587 obtained from The Cancer Genome Atlas6 (TCGute.org). GPX4 and FSP1 (AIFM2) mutational
588 status of TCGA tumor samples was retrieved from cBioPortal151 using the TCGA PanCancer
589 Atlas collection (gdc.cancer.gov/about- data/publications/pancanatlas). For survival data, patients
590 were stratified based on GPX4 or FSP1 expression and overall survival rates were plotted to
591 compare high-GPX4/FSP1 expressing patients (top 50%) with the rest of the cohort (n=464
592 patients). All survival analyses were conducted using the survival curve analyses in GraphPad
593 Prism v9.

594

595 *Statistics*

596 Statistical analysis was performed using GraphPad Prism v9. All data is expressed as mean plus
597 standard error of the mean, unless otherwise specified. Data was analyzed by statistical test
598 indicated in figure legends. All tests were two tailed.
599
600 **Data Availability**
601 Data is available from the corresponding author upon request.
602
603 **Acknowledgements**
604 We dedicate this work to Judy Teixeira, whose love, strength, and spirit continue to inspire us. We
605 thank Gyles Ward and Cynthia Loomis from the Experimental Pathology Core
606 [RRID:SCR_017928], at NYU Langone Health and which is partially supported by the Cancer
607 Center Support Grant P30CA016087 at NYU Langone's Laura and Isaac Perlmutter Cancer Center
608 for support with IHC staining and imaging. The PhenoImagerHT Mutlispectral imaging system
609 was initially purchased through a Shared Instrumentation Grant S10 OD021747. We thank the
610 Wayne State University School of Medicine Lipidomics Core Facility, which is supported in part
611 by National Center for Research Resources, National Institutes of Health Grants S10RR027926
612 and S10OD032292, for support with LC-MS. We also recognize that the analysis of Fsp1 oxidized
613 lipids and $CoQ_9$ were conducted by the Proteomics and Metabolomics Core at the College of
614 Pharmacy, Seoul National University, South Korea. We thank R. Possemato and S. Kotschi for
615 critical reading of this manuscript. T. P. is supported by NIH grants (R37CA222504,
616 R01CA227649, R01CA283049, R01CA262562) and an American Cancer Society Research
617 Scholar Grant (RSG-17-20001–TBE). T.P. received funding from Pfizer Medical Education
618 Group, Dracen Pharmaceuticals, Kymera Therapeutics, Bristol Myers Squibb, and Agios

Pharmaceuticals not related to the submitted work. K.W. is supported by the Ruth L. Kirschstein Individual Predoctoral NRSA fellowship (F30CA275258) and NIH training grants (T32GM136573, T32GM136542). A.J.V. is supported by the NIH training grant (T32GM136542). M.C. received funding from the Deutsche Forschungsgemeinschaft (DFG) (CO 291/7-1, the Priority Program SPP 2306 [CO 291/9-1, #461385412; CO 291/10-1, #461507177] and the European Research Council (ERC) under the European Union's Horizon 2020 research and innovation program (grant agreement No. GA 884754). M.C. is a co-founder and shareholder of ROSCUE Therapeutics GmbH. M.C. and T.N. have filed patents for some of the compounds described herein.

**Author contributions**

T.P., K.W., A.J.V. designed and directed the study. K.W., A.J.V., J.P.B., A.Z., M.N.N., M.M., and S.C. performed various *in vitro* and *in vivo* experiments reported in the study. R.P. performed FACS. Y.H. performed TCGA patient data analyses. S.M.K. performed Fsp1 epilipidomics and COQ measurement, T.H.K assisted with data analysis, and was supervised by Y.P.K. S.C. performed unbiased tumor burden quantification. S.R. maintained and genotyped all experimental mice. M.C., T.N., D.S., M.H., provided conceptual advice. T.P., K.W., and A.J.V. wrote the manuscript with comments and input from all authors.

637 **REFERENCES**


638 1. Dixon, S.J., *et al.* Ferroptosis: an iron-dependent form of nonapoptotic cell death. *Cell* **149**,
639 1060-1072 (2012).
640 2. Wiernicki, B., *et al.* Excessive phospholipid peroxidation distinguishes ferroptosis from
641 other cell death modes including pyroptosis. *Cell Death Dis* **11**, 922 (2020).
642 3. Conrad, M. & Pratt, D.A. The chemical basis of ferroptosis. *Nat Chem Biol* **15**, 1137-1147
643 (2019).
644 4. Dixon, S.J. & Olzmann, J.A. The cell biology of ferroptosis. *Nat Rev Mol Cell Biol* **25**,
645 424-442 (2024).
646 5. Yang, W.S., *et al.* Regulation of ferroptotic cancer cell death by GPX4. *Cell* **156**, 317-331
647 (2014).
648 6. Friedmann Angeli, J.P., *et al.* Inactivation of the ferroptosis regulator Gpx4 triggers acute
649 renal failure in mice. *Nat Cell Biol* **16**, 1180-1191 (2014).
650 7. Doll, S., *et al.* FSP1 is a glutathione-independent ferroptosis suppressor. *Nature* **575**, 693-
651 698 (2019).
652 8. Bersuker, K., *et al.* The CoQ oxidoreductase FSP1 acts parallel to GPX4 to inhibit
653 ferroptosis. *Nature* **575**, 688-692 (2019).
654 9. Kraft, V.A.N., *et al.* GTP Cyclohydrolase 1/Tetrahydrobiopterin Counteract Ferroptosis
655 through Lipid Remodeling. *ACS Cent Sci* **6**, 41-53 (2020).
656 10. Soula, M., *et al.* Metabolic determinants of cancer cell sensitivity to canonical ferroptosis
657 inducers. *Nat Chem Biol* **16**, 1351-1360 (2020).
658 11. Garcia-Bermudez, J., *et al.* Squalene accumulation in cholesterol auxotrophic lymphomas
659 prevents oxidative cell death. *Nature* **567**, 118-122 (2019).
660 12. Qiu, B., *et al.* Phospholipids with two polyunsaturated fatty acyl tails promote ferroptosis.
661 *Cell* **187**, 1177-1190 e1118 (2024).
662 13. Kagan, V.E., *et al.* Oxidized arachidonic and adrenic PEs navigate cells to ferroptosis. *Nat*
663 *Chem Biol* **13**, 81-90 (2017).
664 14. Doll, S., *et al.* ACSL4 dictates ferroptosis sensitivity by shaping cellular lipid composition.
665 *Nat Chem Biol* **13**, 91-98 (2017).
666 15. Dixon, S.J., *et al.* Human Haploid Cell Genetics Reveals Roles for Lipid Metabolism
667 Genes in Nonapoptotic Cell Death. *ACS Chem Biol* **10**, 1604-1609 (2015).
668 16. Mishima, E., *et al.* A non-canonical vitamin K cycle is a potent ferroptosis suppressor.
669 *Nature* **608**, 778-783 (2022).
670 17. Seiler, A., *et al.* Glutathione peroxidase 4 senses and translates oxidative stress into 12/15-
671 lipoxygenase dependent- and AIF-mediated cell death. *Cell Metab* **8**, 237-248 (2008).
672 18. Zilka, O., *et al.* On the Mechanism of Cytoprotection by Ferrostatin-1 and Liproxstatin-1
673 and the Role of Lipid Peroxidation in Ferroptotic Cell Death. *ACS Cent Sci* **3**, 232-243
674 (2017).
675 19. Viswanathan, V.S., *et al.* Dependency of a therapy-resistant state of cancer cells on a lipid
676 peroxidase pathway. *Nature* **547**, 453-457 (2017).
677 20. Hangauer, M.J., *et al.* Drug-tolerant persister cancer cells are vulnerable to GPX4
678 inhibition. *Nature* **551**, 247-250 (2017).
679 21. Berndt, C., *et al.* Ferroptosis in health and disease. *Redox Biol* **75**, 103211 (2024).
680 22. Jiang, X., Stockwell, B.R. & Conrad, M. Ferroptosis: mechanisms, biology and role in
681 disease. *Nat Rev Mol Cell Biol* **22**, 266-282 (2021).

682 23. Nakamura, T., *et al.* Phase separation of FSP1 promotes ferroptosis. *Nature* **619**, 371-377
683 (2023).
684 24. Eaton, J.K., *et al.* Selective covalent targeting of GPX4 using masked nitrile-oxide
685 electrophiles. *Nat Chem Biol* **16**, 497-506 (2020).
686 25. Yang, W.S. & Stockwell, B.R. Synthetic lethal screening identifies compounds activating
687 iron-dependent, nonapoptotic cell death in oncogenic-RAS-harboring cancer cells. *Chem*
688 *Biol* **15**, 234-245 (2008).
689 26. Xavier da Silva, T.N., Schulte, C., Alves, A.N., Maric, H.M. & Friedmann Angeli, J.P.
690 Molecular characterization of AIFM2/FSP1 inhibition by iFSP1-like molecules. *Cell*
691 *Death Dis* **14**, 281 (2023).
692 27. Hendricks, J.M., *et al.* Identification of structurally diverse FSP1 inhibitors that sensitize
693 cancer cells to ferroptosis. *Cell Chem Biol* **30**, 1090-1103 e1097 (2023).
694 28. Nakamura, T., *et al.* Integrated chemical and genetic screens unveil FSP1 mechanisms of
695 ferroptosis regulation. *Nat Struct Mol Biol* **30**, 1806-1815 (2023).
696 29. Yoshioka, H., *et al.* Identification of a Small Molecule That Enhances Ferroptosis via
697 Inhibition of Ferroptosis Suppressor Protein 1 (FSP1). *ACS Chem Biol* **17**, 483-491 (2022).
698 30. Nakamura, T. & Conrad, M. Exploiting ferroptosis vulnerabilities in cancer. *Nat Cell Biol*
699 (2024).
700 31. Sanchez-Rivera, F.J., *et al.* Rapid modelling of cooperating genetic events in cancer
701 through somatic genome editing. *Nature* **516**, 428-431 (2014).
702 32. Ding, H., *et al.* Activation of the NRF2 antioxidant program sensitizes tumors to G6PD
703 inhibition. *Sci Adv* **7**, eabk1023 (2021).
704 33. Lignitto, L., *et al.* Nrf2 Activation Promotes Lung Cancer Metastasis by Inhibiting the
705 Degradation of Bach1. *Cell* **178**, 316-329.e318 (2019).
706 34. Romero, R., *et al.* Keap1 loss promotes Kras-driven lung cancer and results in dependence
707 on glutaminolysis. *Nat Med* **23**, 1362-1368 (2017).
708 35. Best, S.A., *et al.* Distinct initiating events underpin the immune and metabolic
709 heterogeneity of KRAS-mutant lung adenocarcinoma. *Nat Commun* **10**, 4190 (2019).
710 36. Takahashi, N., *et al.* 3D Culture Models with CRISPR Screens Reveal Hyperactive NRF2
711 as a Prerequisite for Spheroid Formation via Regulation of Proliferation and Ferroptosis.
712 *Mol Cell* **80**, 828-844 e826 (2020).
713 37. Zou, Y., *et al.* A GPX4-dependent cancer cell state underlies the clear-cell morphology and
714 confers sensitivity to ferroptosis. *Nat Commun* **10**, 1617 (2019).
715 38. Vidigal, J.A. & Ventura, A. Rapid and efficient one-step generation of paired gRNA
716 CRISPR-Cas9 libraries. *Nat Commun* **6**, 8083 (2015).
717 39. Ingold, I., *et al.* Selenium Utilization by GPX4 Is Required to Prevent Hydroperoxide-
718 Induced Ferroptosis. *Cell* **172**, 409-422 e421 (2018).
719 40. Cancer Genome Atlas Research, N. Comprehensive molecular profiling of lung
720 adenocarcinoma. *Nature* **511**, 543-550 (2014).
721 41. Muller, F., *et al.* Elevated FSP1 protects KRAS-mutated cells from ferroptosis during
722 tumor initiation. *Cell Death Differ* **30**, 442-456 (2023).
723 42. Koppula, P., *et al.* A targetable CoQ-FSP1 axis drives ferroptosis- and radiation-resistance
724 in KEAP1 inactive lung cancers. *Nat Commun* **13**, 2206 (2022).
725 43. Zavitsanou, A.M., *et al.* KEAP1 mutation in lung adenocarcinoma promotes immune
726 evasion and immunotherapy resistance. *Cell Rep* **42**, 113295 (2023).

727 44. Wu, K., El Zowalaty, A.E., Sayin, V.I. & Papagiannakopoulos, T. The pleiotropic
728 functions of reactive oxygen species in cancer. *Nat Cancer* **5**, 384-399 (2024).
729 45. Cheung, E.C. & Vousden, K.H. The role of ROS in tumour development and progression.
730 *Nat Rev Cancer* **22**, 280-297 (2022).
731 46. Yant, L.J.*, et al.* The selenoprotein GPX4 is essential for mouse development and protects
732 from radiation and oxidative damage insults. *Free Radic Biol Med* **34**, 496-502 (2003).
733 47. Mei, J., Webb, S., Zhang, B. & Shu, H.B. The p53-inducible apoptotic protein AMID is
734 not required for normal development and tumor suppression. *Oncogene* **25**, 849-856
735 (2006).
736 48. Nguyen, H.P.*, et al.* Aifm2, a NADH Oxidase, Supports Robust Glycolysis and Is Required
737 for Cold- and Diet-Induced Thermogenesis. *Mol Cell* **77**, 600-617 e604 (2020).
738 49. Drijvers, J.M.*, et al.* Pharmacologic Screening Identifies Metabolic Vulnerabilities of
739 CD8(+) T Cells. *Cancer Immunol Res* **9**, 184-199 (2021).
740 50. Matsushita, M.*, et al.* T cell lipid peroxidation induces ferroptosis and prevents immunity
741 to infection. *J Exp Med* **212**, 555-568 (2015).
742 51. Criscuolo, A.*, et al.* Analytical and computational workflow for in-depth analysis of
743 oxidized complex lipids in blood plasma. *Nature Communications* **13**, 6547 (2022).
744 52. Goracci, L.*, et al.* Lipostar, a Comprehensive Platform-Neutral Cheminformatics Tool for
745 Lipidomics. *Analytical Chemistry* **89**, 6257-6264 (2017).
746 53. Adams, K.J.*, et al.* Skyline for Small Molecules: A Unifying Software Package for
747 Quantitative Metabolomics. *Journal of Proteome Research* **19**, 1447-1458 (2020).
748 54. Kang, Y.P., Kim, T.H., Ngoc Nguyen, C.T., Kim, S.M. & Kwon, S.W. Robust
749 Determination of Coenzyme Q10 Redox Status Using Two Isotope-Labeled Internal
750 Standards. *Available at SSRN 4982487*.
751
752

753 **Figure Legends**

754 **Fig. 1: Gpx4 loss triggers ferroptosis in lung tumors**

755 **(a)** Schematic of KP LUAD GEMMs intratracheally infected with pUSEC lentiviruses containing
756 dual sgRNAs targeting Neo (control; n=14) or Gpx4 (n=13). Mice were dosed with Liproxstatin-
757 1 (LIP1; n=7 per genotype) or Vehicle (Veh; n=6 sgNeo, n=7 sgGpx4) every other day starting
758 from tumor initiation to experiment endpoint. **(b)** Tumor burden quantification of KP LUAD
759 tumors with knockout of either control (sgNeo) or Gpx4 (sgGpx4) and treated with Veh or LIP1.
760 **(c)** Representative MRI of KP LUAD tumors with knockout of either control or Gpx4 and treated
761 with Veh or LIP1. **(d)** Representative H&E of KP LUAD tumors with knockout of either control
762 or Gpx4 and treated with Veh or LIP1. **(e)** Tumor 4-HNE IHC quantification of KP LUAD tumors
763 with knockout of either control or Gpx4 and treated with Veh or LIP1. **(f)** Representative 4-HNE
764 IHC of KP LUAD tumors with knockout of either control or Gpx4 and treated with Veh or LIP1.
765 Error bars represent SEM values, significance was determined via one-way ANOVA (panels b, e).
766

767 **Fig. 2: Fsp1 knockout robustly restricts lung tumorigenesis**

768 **(a)** Schematic depicting mechanisms of Fsp1- and Gpx4-mediated buffering against cellular lipid
769 peroxidation/ferroptosis. **(b)** Overall survival of KRAS-mutant LUAD patients (n=280) from
770 TCGA, stratified by high versus low primary tumor FSP1 (AIFM2) expression. Median survival
771 for FSP1 high (1215 days) versus FSP1 low (1498 days). **(c)** Representative IHC staining for Fsp1
772 and Gpx4 in adenoma versus adenocarcinoma KP LUAD GEMM tumors. **(d)** Tumor Fsp1 IHC
773 quantification of KP LUAD GEMM tumors at 10- versus 14-weeks post tumor initiation. **(e)**
774 Schematic of KP LUAD GEMMs intratracheally infected with pUSEC lentiviruses containing
775 double sgRNAs targeting Neo (control; n=4), Fsp1 (n=6), or Gpx4 (n=6). **(f)** Tumor burden

776 quantification of KP LUAD tumors with knockout of either control (Neo), Fsp1, or Gpx4. **(g)**
777 Representative H&E of KP LUAD tumors with knockout of either control (Neo), Fsp1, or Gpx4.
778 **(h)** Quantification of relative proportion of adenomas versus adenocarcinomas of KP LUAD
779 tumors with knockout of either control (Neo), Fsp1, or Gpx4. **(i)** Representative TUNEL staining
780 of KP, Fsp1KO and Fsp1WT orthotopic lung tumors **(j)** Schematic depicting generation of
781 isogenic Fsp1-wildtype (Fsp1WT) versus Fsp1-knockout (Fsp1KO) cells for paralleled *in vitro*
782 assays and *in vivo* syngeneic orthotopic transplantation studies. **(k)** Representative images of
783 crystal violet clonogenic growth assay in isogenic KP, Fsp1KO and Fsp1WT cells treated with
784 RSL3 (0.5μM) ± LIP1 (100nM). **(l)** Tumor burden quantification of KP, Fsp1KO (n=8) and
785 Fsp1WT (n=7) orthotopic lung tumors. **(m)** Representative H&E of KP, Fsp1KO and Fsp1WT
786 orthotopic lung tumors. Error bars represent SEM values, significance was determined via
787 student's t-test (panels d and l) or one-way ANOVA (panel f) or Kaplan-Meier simple survival
788 analysis (panel b).
789
790 **Fig. 3: Sensitivity to FSP1 loss is not dependent on tumor mutations or lineage**
791 Longitudinal growth and endpoint weights from indicated cell lines with CRISPR/Cas9-mediated
792 knockout of FSP1 or non-targeting controls, transplanted as subcutaneous (subQ) xenograft tumors
793 into NSG mice: **(a)** H2009, FSP1 (n=8) or control (n=8). **(b)** H1299, FSP1 (n=9) or control (n=9).
794 **(c)** PC9, FSP1 (n=9) or control (n=9). **(d)** H1975, FSP1 (n=8) or control (n=9). **(e)** A549, FSP1
795 (n=10) or control (n=9). **(f)** 16645, Fsp1(n=7) or control (n=9). **(g)** KPC7 (murine PDAC), Fsp1
796 (n=10) or control (n=10). Error bars represent SEM values, significance was determined via
797 student's t test (panels a-g)
798

799 **Fig. 4: FSP1 is required for the suppression of ferroptosis *in vivo***

800 **(a)** Heatmap of indicated oxidized PE/PC lipid species detected via LC/MS from KP, Fsp1KO and
801 Fsp1WT orthotopic tumors. **(b)** Longitudinal growth of KP, Gpx4KO or Fsp1OE subcutaneous
802 (subQ) xenograft tumors transplanted in male C57BL/6J mice. (control, n=9, Fsp1OE, n=8) **(c)**
803 Longitudinal growth of KP, Fsp1KO, Fsp1WT, or Gpx4OE subQ xenograft tumors transplanted
804 in female C57BL/6J mice. (control, n=10, controlOE, n=9, Fsp1WT, n=9, Gpx4OE, n=8). **(d)**
805 Ratio of CoQ9H2/CoQ9 detected via LC/MS from KP, Fsp1KO, Fsp1WT orthotopic tumors and
806 cells treated with DMSO or RSL3 (0.5 μM) for 8 hours. **(e)** Schematic depicting Acsl4's pro-
807 ferroptotic function, counteracted by ferroptosis suppressors like Fsp1 and lipid radical-trapping
808 antioxidants (RTAs) such as Vitamin E (VitE) and Liproxstatin-1 (LIP1). **(f)** Tumor burden
809 quantification of KP, Fsp1KO and Fsp1WT orthotopic lung tumors with CRISPR/Cas9-mediated
810 knockout of Acsl4 or control (Neo). (WT, n=5; Acsl4KO, n=4; Fsp1KO, n=7; Fsp1KOAcsl4KO,
811 n=7). **(g)** Schematic depicting dietary Vitamin E (VitE) manipulation studies. **(h)** Tumor
812 bioluminescence signal normalized to first imaging timepoint of C57BL/6J mice orthotopically
813 transplanted with KP, Fsp1KO cells and receiving high (n=8) or low (n=7) VitE diets *ad libitum*
814 5 days pre-tumor initiation. **(i)** Tumor bioluminescence signal of C57BL/6J mice orthotopically
815 transplanted with KP, Fsp1KO cells and placed on high (n=6) or low (n=6) VitE diets *ad libitum*
816 after lung tumor establishment (day18). **(j)** Schematic of KP LUAD GEMMs intratracheally
817 infected with pUSEC lentiviruses containing double sgRNAs targeting Neo (control, n=12) or
818 Fsp1 (n=12). Mice were dosed with Liproxstatin-1 (LIP1, n=6 per genotype) or Vehicle (Veh, n=6
819 per genotype) every other day starting 5 weeks post-tumor initiation until experiment endpoint.
820 **(k)** Tumor burden quantification of KP LUAD tumors with knockout of either control or
821 Fsp1 and treated with Veh or LIP1. **(l)** Representative H&E of KP LUAD tumors with knockout

822 of either control or Fsp1 and treated with Veh or LIP1. Error bars represent SEM values,
823 significance was determined via student's t test (panel b), one-way ANOVA (panels c, d, f, k), or
824 Tukey's multiple comparison (panel h, i).
825
826 **Fig. 5: FSP1 is a viable therapeutic target for *KRAS*-mutant lung adenocarcinoma**
827 **(a)** Overall survival of C57BL/6J mice with orthotopic lung tumors with Fsp1KO (n=7) or hFSP1
828 re-expression, treated with icFSP1 (n=8) or Vehicle (n=7). **(b)** Tumor bioluminescence signal of
829 C57BL/6J mice orthotopically transplanted with hFsp1WT cells and treated with either Vehicle
830 (n=8), LIP1 (n=7), icFSP1 (n=8), or icFSP1+LIP1 (n=8). **(c)** Overall survival of C57BL/6J mice
831 with Fsp1KO (n=5), hFSP1WT, or hFSP1Q319K-expressing tumors, treated with icFSP1
832 (hFSP1WT, n=6; hFSP1Q319K, n=7) or Vehicle (hFSP1WT, n=7; hFSP1Q319K, n=7). **(d)**
833 Longitudinal growth of PDX LX465 tumors treated with icFSP1 (n=10) or Vehicle (n=10) in NSG
834 mice. Error bars represent SEM values, significance was determined via one-way ANOVA (panel
835 b), student's t-test (panel d), or Kaplan-Meier simple survival analysis (panels a and c).
836

837 **Extended Data Figure Legends**

838 **Extended Data Fig. 1: Gpx4 is required by lung cancer cells**

839 (a) Quantification and representative images of Gpx4 IHC in KP LUAD GEMM tumors with
840 knockout of either control (sgNeo, n=11) or Gpx4 (n=12). (b) Representative 4-HNE IHC of liver
841 tissue from conditional Gpx4-knockout mice. (c) Top: Western blot of KP LUAD cells with
842 CRISPR/Cas9-mediated genetic deletion of Gpx4 with either two individual or duplexed sgRNAs.
843 Bottom: Representative images of crystal violet clonogenic assay of KP LUAD cells with
844 knockout of either control (sgNeo) or Gpx4. Cells were treated with 100nM LIP1. (d) Heatmap of
845 LC-MS detection of oxidized phospholipids in KP LUAD cells treated with DMSO control, RSL3
846 (0.5μM), and RSL3 (0.5μM) + LIP1 (100nM) for 8 hours. (e) Schematic of Gpx4 ectopic
847 overexpression (OE) method in KP LUAD cells. Western blot and representative images of
848 crystal violet clonogenic assay of KP LUAD cells with wildtype (WT) or OE of Gpx4. (f)
849 CellTiter-Glo Luminescence viability assay of KP, Gpx4 WT or OE cells upon increasing
850 concentrations of RSL3. (g) Western blot of KP LUAD cells treated with 20nM Na2SeO3 or
851 DMSO. CellTiter-Glo Luminescence viability assay of KP LUAD cells treated with 20nM
852 Na2SeO3 or DMSO with increasing RSL3 addition. (h) GPX4 expression of *KRAS*-mutant
853 primary LUAD tumors from TCGA, divided into early and late tumor stages. (i) Overall survival
854 of *KRAS*-mutant LUAD patients (n=464) from TCGA, stratified by high vs low tumor GPX4
855 expression. (j) Tumor Gpx4 IHC quantification of KP LUAD GEMM tumors at 10 wks (n=4) vs
856 14 wks (n=4) post-tumor initiation. Error bars represent SEM values, significance was determined
857 via one-way ANOVA (panel h) or student's t-test (panel j) or Kaplain-Meier simple survival
858 analysis (panel i). Box plots indicate median (middle line), 25th, 75th percentile (box) and 5th and
859 95th percentile (whiskers).

860 **Extended Data Fig. 2: FSP1's anti-ferroptotic function is not dependent on oncogenic**
861 **signaling**

862 **(a)** FSP1 (AIFM2) expression of *KRAS*-mutant primary LUAD tumors from TCGA, divided into
863 early and late tumor stages. **(b)** FSP1 (AIFM2) expression of *KRAS*-mutant primary LUAD tumors
864 from TCGA, separated by the *KRAS* mutation (G12C n=51, G12V n=32, G12D n=17, G12A n=16,
865 Other KRAS n=20). **(c)** FSP1 (AIFM2) expression of primary LUAD tumors from TCGA,
866 separated by oncogenic driver mutation (normal lung, n=59, EGFR, n=71, KRAS, n=135, Other,
867 n=307). **(d)** Western blot of KP human cells treated with 50 nm RMC-042 for indicated time
868 periods. **(e)** Representative multi-IF images of KP tumors using indicated antibodies. Panels are
869 10X and insets are 20X. **(f)** FSP1 (AIFM2) expression of KRAS-mutant primary LUAD tumors
870 from TCGA, separated by the co-mutation status of the tumor (KEAP1/STK11 WT n=88, STK11
871 mutant n=20, KEAP1 mutant n=16, KEAP1/STK11 mutant n=11). **(g)** QPCR of FSP1 (AIFM2)
872 expression from indicated human cell lines treated with KI696 for 5 days. Error bars represent
873 SEM values, significance was determined by one-way ANOVA (panels a, b, c, f, g). Box plots
874 indicate median (middle line), 25th, 75th percentile (box) and 5th and 95th percentile (whiskers).
875

876 **Extended Data Fig. 3: Neither Fsp1 nor Gpx4 have an impact on tumor initiation,**
877 **proliferation, or apoptosis**

878 **(a)** Quantification and representative images of tumor Fsp1 IHC in KP LUAD GEMM tumors
879 with knockout of either control (sgNeo, n=11) or Fsp1 (n=14). **(b)** Tumor number quantification
880 in KP LUAD GEMMs with tumor-specific knockout of either control (sgNeo, n=4), Fsp1 (n=7),
881 or Gpx4 (n=6). **(c)** Tumor burden quantification of KP LUAD tumors with knockout of either
882 control (Neo), Fsp1, or Gpx4. Data is plotted with the area of individual tumors as each data point.

883 **(d)** Ki67 IHC quantification of KP LUAD GEMM tumors with knockout of either control, Fsp1,
884 or Gpx4. **(e)** Cleaved caspase-3 IHC quantification of KP LUAD GEMM tumors with knockout
885 of either control, Fsp1, or Gpx4. Error bars represent SEM values, significance was determined by
886 one-way ANOVA (panels b-e).
887
888 **Extended Data Fig. 4: Fsp1 is required for cell-autonomous tumor growth *in vivo***
889 **(a)** Top: Western blot of KP LUAD cells with CRISPR/Cas9-mediated genetic deletion of Fsp1
890 with either two individual or duplexed sgRNAs. Bottom: Representative images of crystal violet
891 clonogenic assay of KP LUAD cells with knockout of either control (sgNeo) or Fsp1. Cells were
892 treated with 100nM LIP1. **(b)** Schematic depicting all transplantation models performed using
893 isogenic KP, Fsp1KO and Fsp1WT **(c, d)** Longitudinal growth and endpoint weights of KP LUAD
894 cells with CRISPR/Cas9-mediated knockout of Fsp1 (n=8) or control (n=10) subcutaneous (subQ)
895 xenograft tumor transplanted into C57BL/6J male mice. **(e)** Tumor bioluminescence signal of
896 C57BL/6J male mice with orthotopic transplantation of KP LUAD cells with CRISPR/Cas9-
897 mediated knockout of Fsp1 (n=8) or control (n=7). **(f)** Tumor bioluminescence signal normalized
898 to initial IVIS timepoint (day 7) of C57BL/6J male mice with orthotopic transplantation of isogenic
899 KP, Fsp1KO (n=6) and Fsp1WT (n=7) cells. **(g)** Tumor bioluminescence signal of NU/J
900 immunocompromised mice with orthotopic transplantation of isogenic KP, Fsp1KO (n=6) and
901 Fsp1WT (n=7) cells. **(h)** Tumor bioluminescence signal of C57BL/6J female mice with orthotopic
902 transplantation of isogenic KP, Fsp1KO (n=8) and Fsp1WT (n=8) cells. **(i)** Longitudinal growth
903 and endpoint tumor weight of either Fsp1KO or Fsp1WT subcutaneous (subQ) xenograft tumors
904 transplanted in C57BL/6J WT (KO, male n=10, female n=10, WT, male n=8, female n=10) or
905 C57BL/6J Fsp1 KO mice (males and females, KO, n=12, WT, n=10). **(j)** Western blot of KP

906 LUAD cells with wildtype (WT) or overexpression (OE) of Fsp1. Representative images
907 of crystal violet clonogenic assay of KP LUAD cells with WT or OE of Fsp1. **(k)** CellTiter-Glo
908 Luminescence viability assay of KP, Fsp1 WT or OE cells with increasing concentrations of RSL3.
909 **(l, m)** Longitudinal growth and endpoint weights of KP LUAD cells with OE (n=10) or WT (n=10)
910 Fsp1-expressing subcutaneous (subQ) xenograft tumor transplanted into C57BL/6J male mice.
911 Error bars represent SEM values, significance determined via one-way ANOVA (panel i), Tukeys
912 multiple comparisons test (panels c, e, f, g, h, l), or student's t-test (panel d, m).
913
914 **Extended Data Fig. 5: FSP1 loss *in vitro* does not induce ferroptosis without RSL3**
915 **(a)** Top: Western blot; Bottom: baseline growth (normalized to control); and Right: CellTiter-Glo
916 Luminescence viability assay of H2009 cells with the lentiviral addition of Cas9 and guide RNAs
917 targeting FSP1 or a non-targeting control (TOM). Viability assay is upon increasing concentrations
918 of RSL3. **(b)** As in (a), but with H1299 cells. **(c)** As in (a), but with PC9 cells. **(d)** As in (a), but
919 with H1975 cells. **(e)** As in (a), but with A549 cells. **(f)** As in (a), but with 16645 cells. **(g)** As in
920 (a), but with KPC7 cells. Error bars represent SEM values, significance was determined via
921 student's t-test (panels a-g).
922
923 **Extended Data Fig. 6: Fsp1 loss promotes tumor cell ferroptosis**
924 **(a)** Western blot of KP, Gpx4KO LUAD cells with either empty vector (—), Fsp1OE. **(b)** Western
925 blot of KP, Fsp1KO LUAD cells with re-expression of either empty vector (—), Fsp1WT,
926 Gpx4OE. **(c)** CellTiter-Glo Luminescence viability assay of KP, Fsp1KO LUAD cells in (b) upon
927 increasing concentrations of RSL3. **(d)** Endpoint tumor weights from indicated cell lines
928 transplanted as subcutaneous (subQ) xenograft tumors in C57BL/6J female mice. **(e)** Top: Western

929 blot of KP, Fsp1KO LUAD cells with re-expression of either empty vector (—), wildtype (WT)
930 Fsp1, or mutant (mut) Fsp1. Bottom: Representative images of crystal violet clonogenic assay. **(f)**
931 CellTiter-Glo Luminescence viability assay of KP, Fsp1KO LUAD cells with re-expression of
932 either empty vector (Fsp1KO), Fsp1WT, or Fsp1mut upon increasing concentrations of RSL3.
933 LIP1 was used at 100nM. **(g)** Tumor bioluminescence signal normalized to initial imaging
934 timepoint (day14) of C57BL/6J male mice with orthotopic transplantation of isogenic KP, Fsp1KO
935 LUAD cells with re-expression of either empty vector (Fsp1KO), Fsp1WT, or Fsp1mut. **(h)**
936 Representative images of crystal violet clonogenic assay of KP, Fsp1WT or Fsp1KO LUAD cells
937 with CRISPR/Cas9- mediated knockout of control (Neo) or Acsl4. **(i)** Tumor bioluminescence
938 signal of C57BL/6J male mice with orthotopic transplantation of isogenic KP, Fsp1KO and
939 Fsp1WT cells with CRISPR/Cas9-mediated knockout of control (Neo) or Acsl4. (WT, n=5;
940 Acsl4KO, n=4; Fsp1KO, n=7; Fsp1KOAcsl4KO, n=7). **(j)** Representative H&E of experiment in
941 (i). **(k)** Overall survival of C57BL/6J male mice with orthotopic transplantation of isogenic KP,
942 Fsp1KO and Fsp1WT cells with CRISPR/Cas9-mediated knockout of control (Neo) or Acsl4
943 (n=5). **(l)** Tumor bioluminescence signal normalized to first imaging timepoint (day7) of
944 C57BL/6J mice orthotopically transplanted with KP, Fsp1WT cells and receiving high (n=6) or
945 low (n=5) VitE diets *ad libitum* 5 days pre-tumor initiation. **(m)** Tumor bioluminescence signal
946 normalized to first imaging timepoint (day7) of C57BL/6J mice orthotopically transplanted with
947 KP, Fsp1KO cells and receiving Liproxstatin-1 (LIP1, n=7) or Vehicle (n=6) daily after tumor
948 establishment. **(n)** Schematic of KP LUAD GEMMs intratracheally infected with pUSEC
949 lentiviruses containing dual sgRNAs targeting Fsp1. Mice were dosed with LIP1 (n=6) or Vehicle
950 (Veh, n=7) every other day starting from tumor initiation. **(o)** Tumor burden quantification of KP
951 LUAD GEMM tumors with knockout of Fsp1 and treated with Veh or LIP1. **(p)** Representative

952 H&E and 4-HNE IHC of KP LUAD GEMM tumors with knockout of Fsp1 and treated with Veh
953 or LIP1. Error bars represent SEM values, significance was determined via one-way ANOVA
954 (panel d), Tukey's multiple comparisons test (g, i, l, m) or student's t-test (panel o) or Kaplain-
955 Meier simple survival analysis (panel k).
956
957 **Extended Data Fig. 7: icFSP1 exerts on-target tumor-suppressive effect**
958 **(a)** Top: Western blot of KP, Fsp1KO LUAD cells with re-expression of either empty vector (—),
959 wildtype (WT) hFSP1, or Q319K-mutant hFSP1. Bottom: Representative images of crystal violet
960 clonogenic assay. **(b)** Cell-TiterGlo Luminescence viability assay of KP, Fsp1KO LUAD cells
961 with re-expression of either empty vector (—), WT hFSP1, or Q319K-mutant hFSP1. **(c)** CellTiter-
962 Glo Luminescence viability assay of human or mouse Fsp1WT-expressing cells upon RSL3
963 (0.2μM) plus increasing concentrations of iFSP1. **(d)** CellTiter-Glo Luminescence viability assay
964 as in (h) but with FSEN1. **(e)** CellTiter-Glo Luminescence viability assay of human or mouse
965 Fsp1WT-expressing cells upon increasing concentrations of icFSP1. **(f)**CellTiter-Glo
966 Luminescence viability assay of WT or Q319K-mutant hFSP1-expressing cells upon RSL3
967 (0.2μM) plus increasing concentrations of icFSP1. **(g)** Tumor bioluminescence signal normalized
968 to first imaging timepoint (day7) of C57BL/6J mice orthotopically transplanted with isogenic KP,
969 Fsp1KO cells with re-expression of either human (hFSP1, n=5) or mouse FSP1 (mFsp1, n=6)
970 cDNA or control (ctrl, n=6) vector. **(h)** Tumor burden quantification and representative H&E of
971 KP, Fsp1KO and hFSP1WT orthotopic lung tumors. **(i)** Representative H&E of KP, hFSP1WT
972 orthotopic lung tumors from indicated treatment groups. **(j)** Percent of T-cells, alveolar, interstitial
973 macrophages, and neutrophils of total CD45+ cells from tumor bearing lungs treated with the
974 indicated compounds for two weeks (Veh, n=7, LIP1, n=7, icFSP1, n=9, icFSP1+LIP1,n=6). **(k)**

975 Graphical summary depicting ferroptosis as a barrier to lung cancer, as loss of either Fsp1 or Gpx4
976 induces tumor cell ferroptosis and restricts disease progression. **(l)** Table of the respective
977 mutations and tumor type of the cell lines used in this work. Error bars represent SEM values,
978 significance was determined via one-way ANOVA (panels g, j) or student's t test (panel h).

# Fig. 1: Gpx4 loss triggers ferroptosis in lung tumors

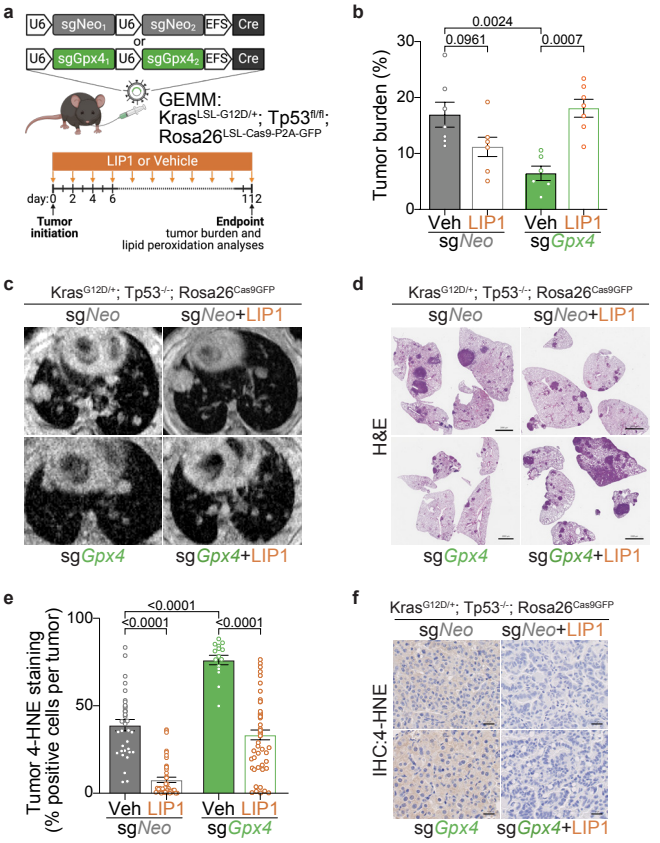

# Fig. 2: Fsp1 knockout robustly restricts lung tumorigenesis

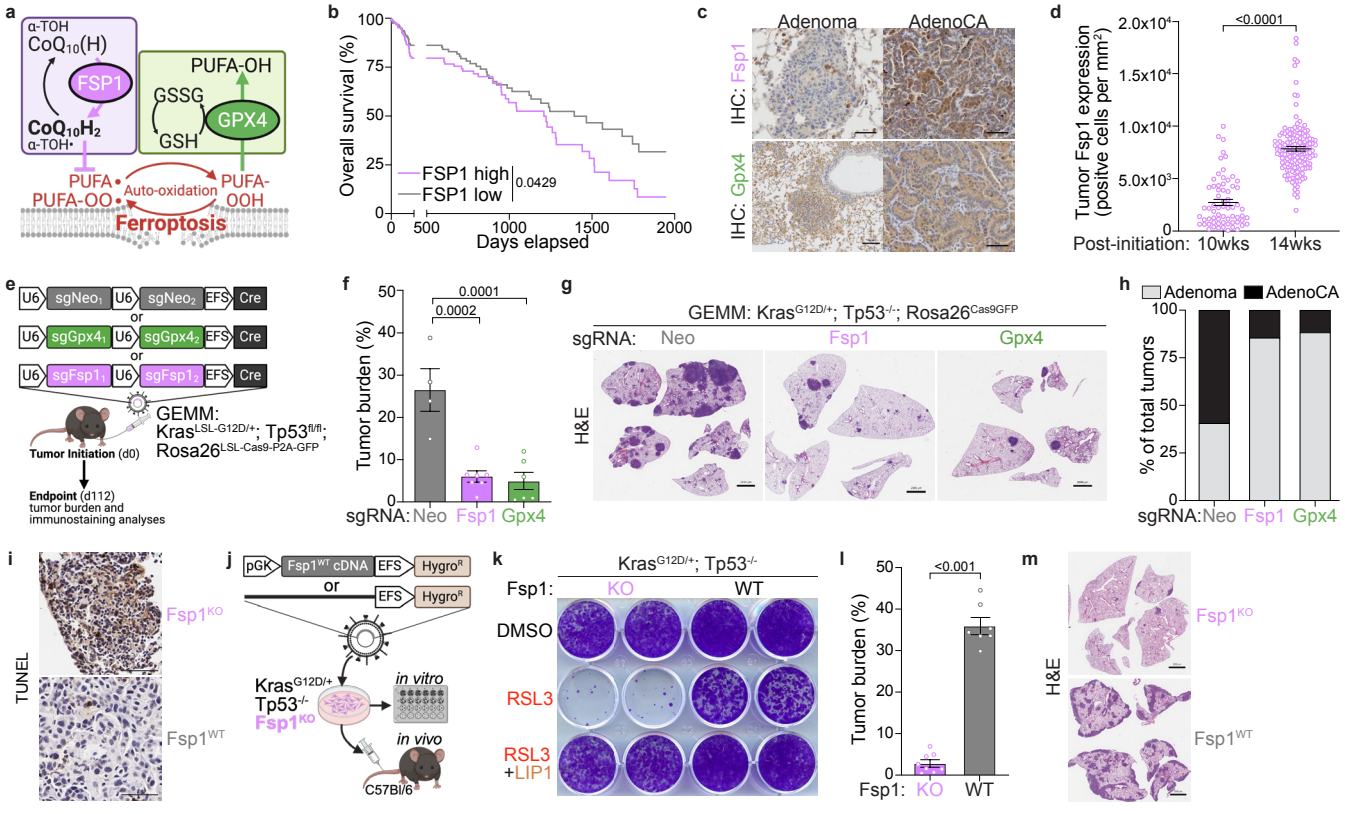

# Fig. 3: Sensitivity to FSP1 loss is not dependent on tumor mutations or lineage

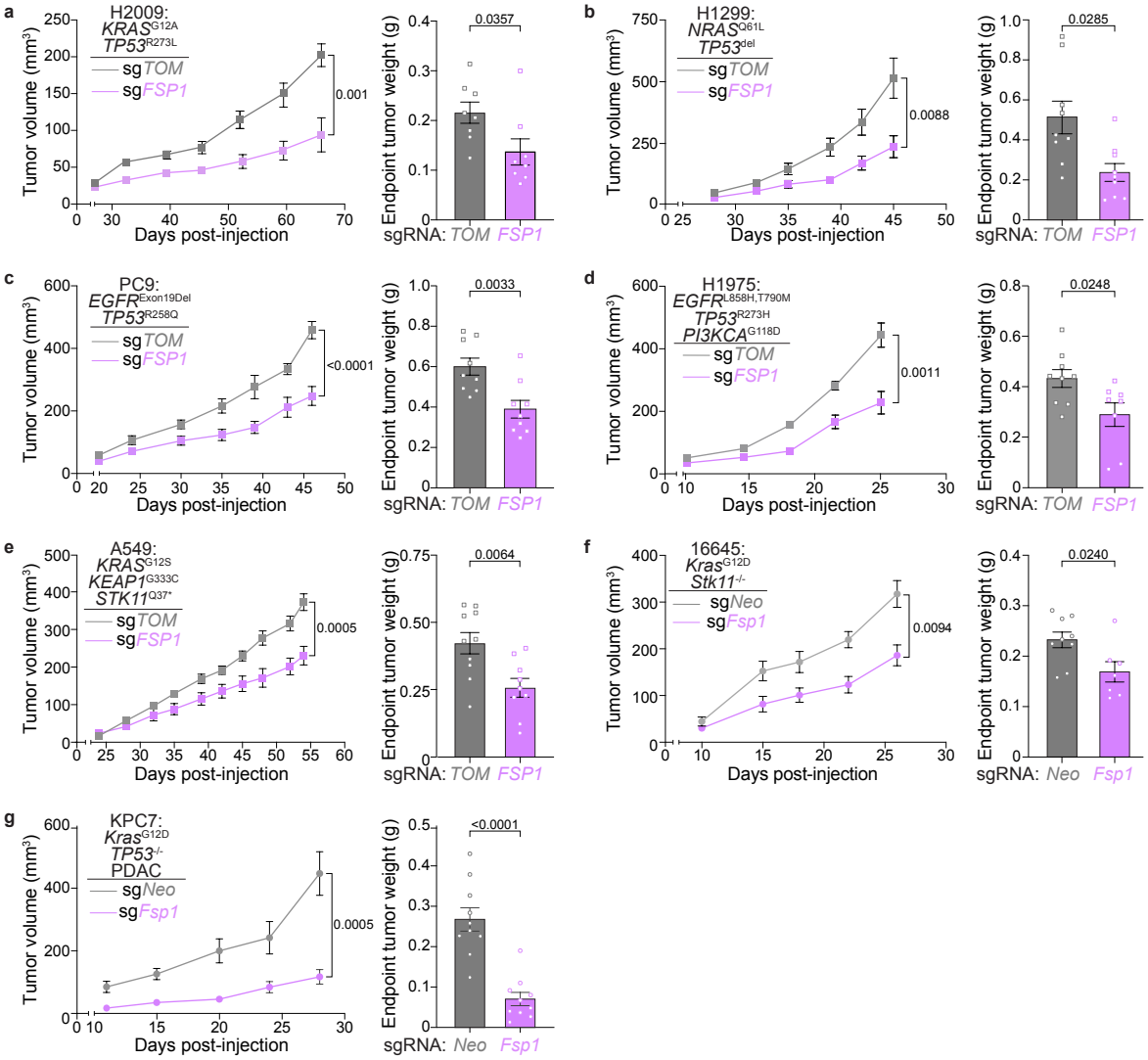

# Fig. 4: FSP1 is required for the suppression of ferroptosis *in vivo*

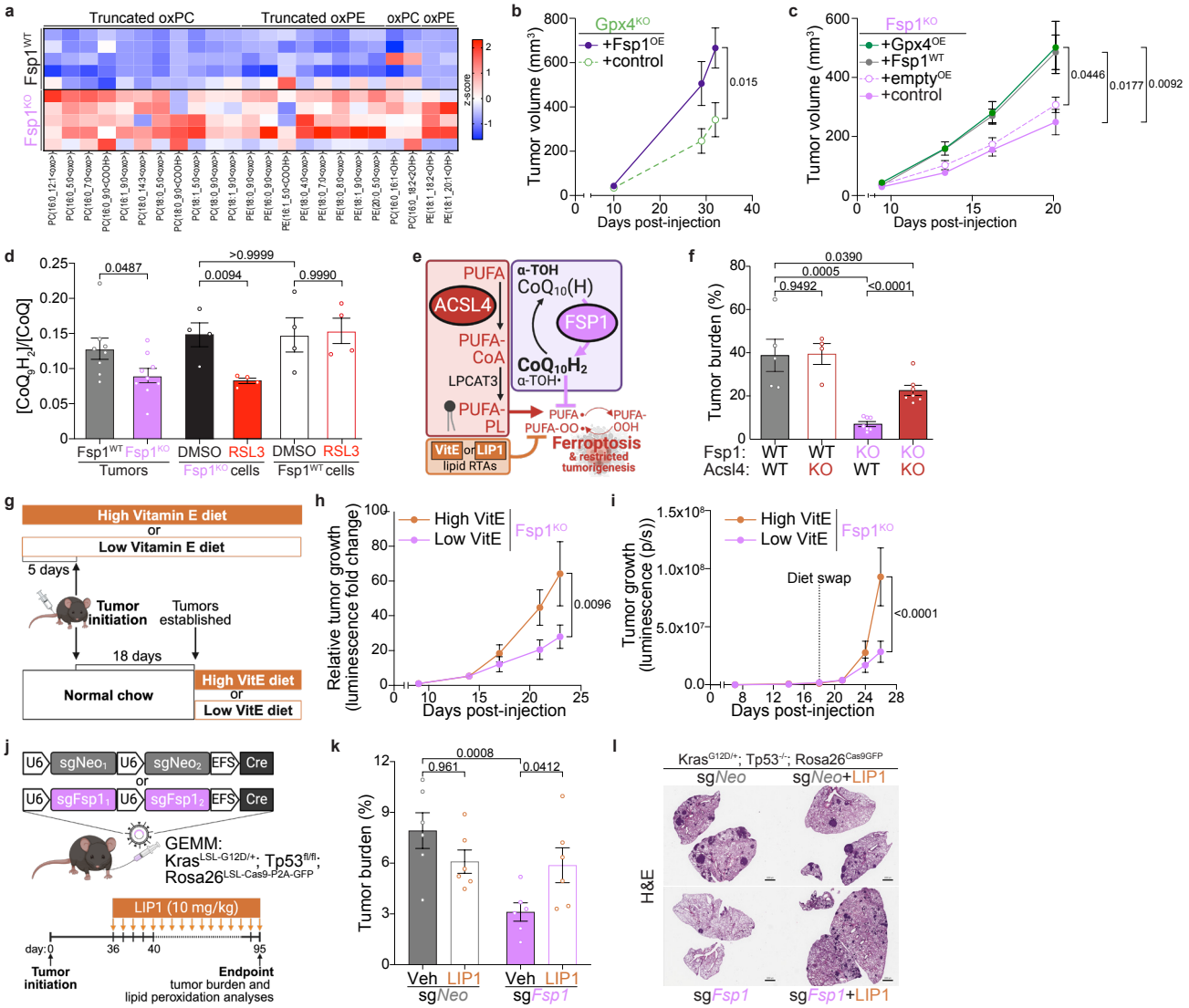

**Fig. 5: FSP1 is a viable therapeutic target for *KRAS*-mutant lung adenocarcinoma**

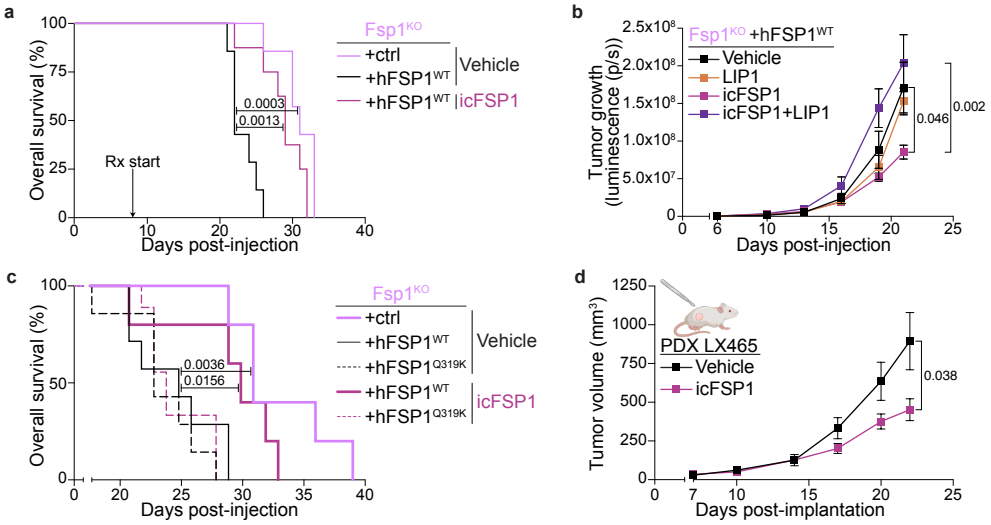

# Extended Data Fig. 1: Gpx4 is required by lung cancer cells

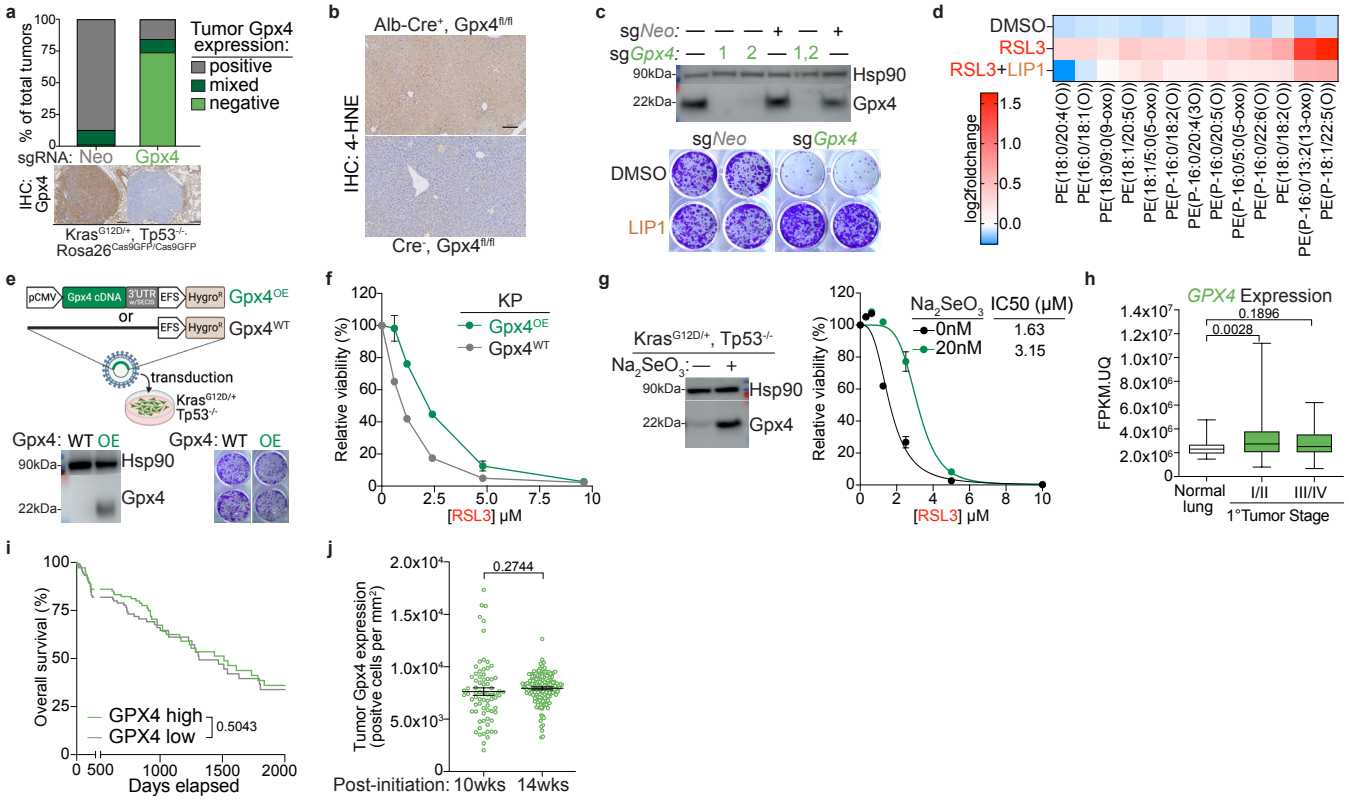

# Extended Data Fig. 2: FSP1's anti-ferroptotic function is not dependent on oncogenic signaling

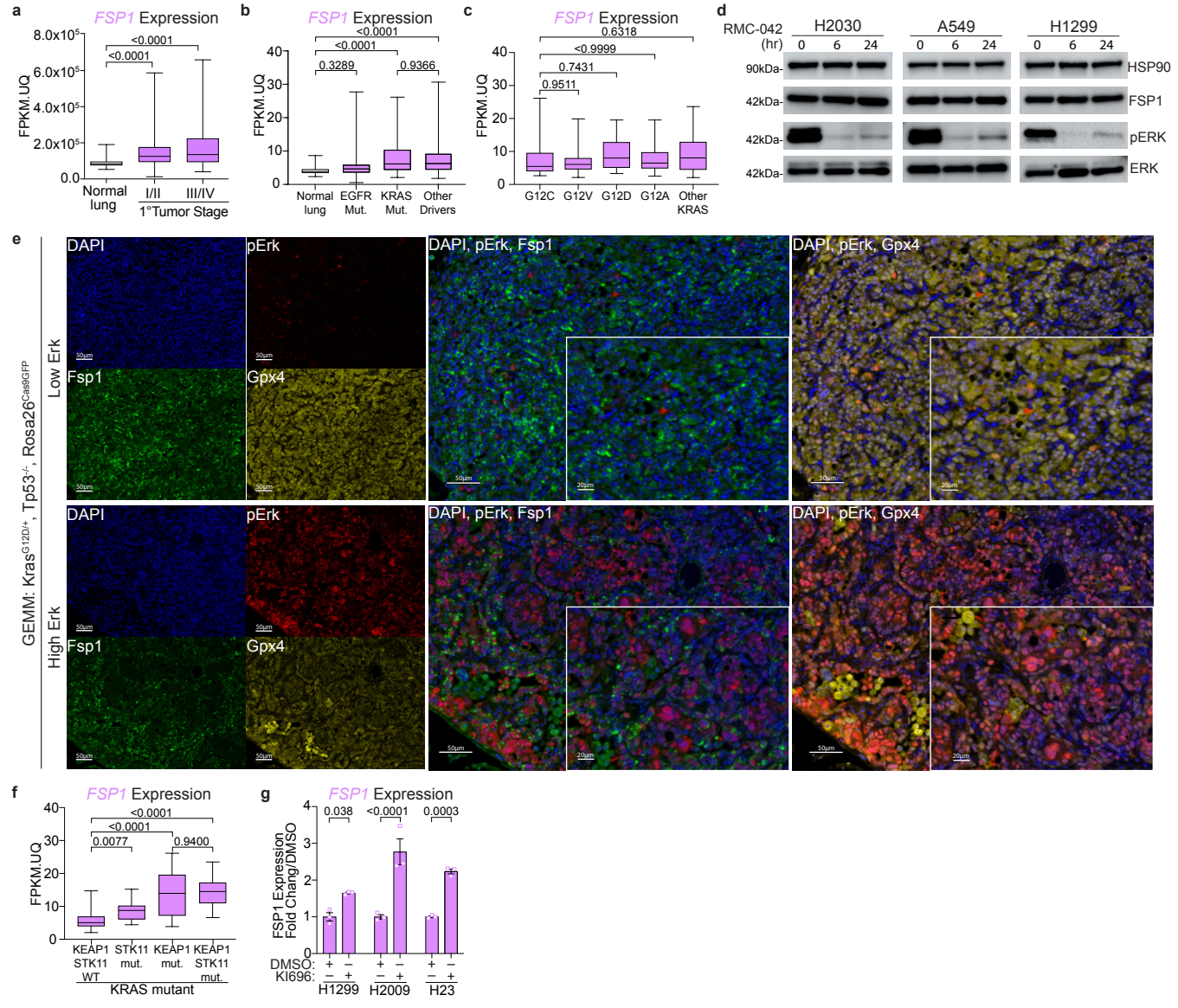

# Extended Data Fig. 3: Neither Fsp1 nor Gpx4 have an impact on tumor initiation, proliferation, or apoptosis

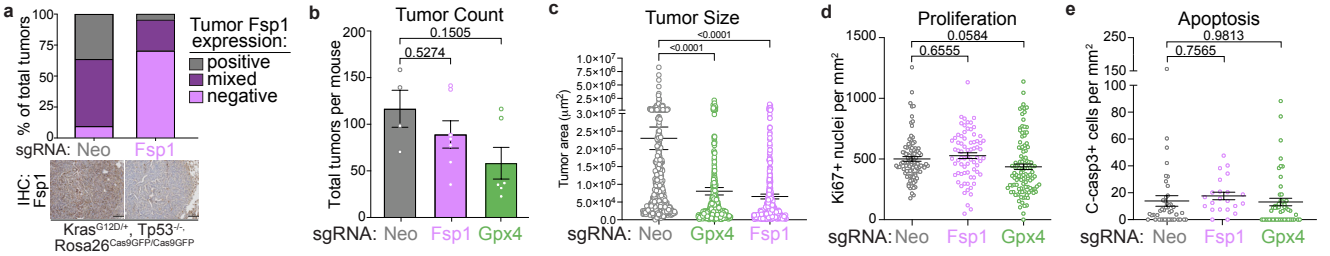

# Extended Data Fig. 4: Fsp1 is required for cell-autonomous tumor growth *in vivo*

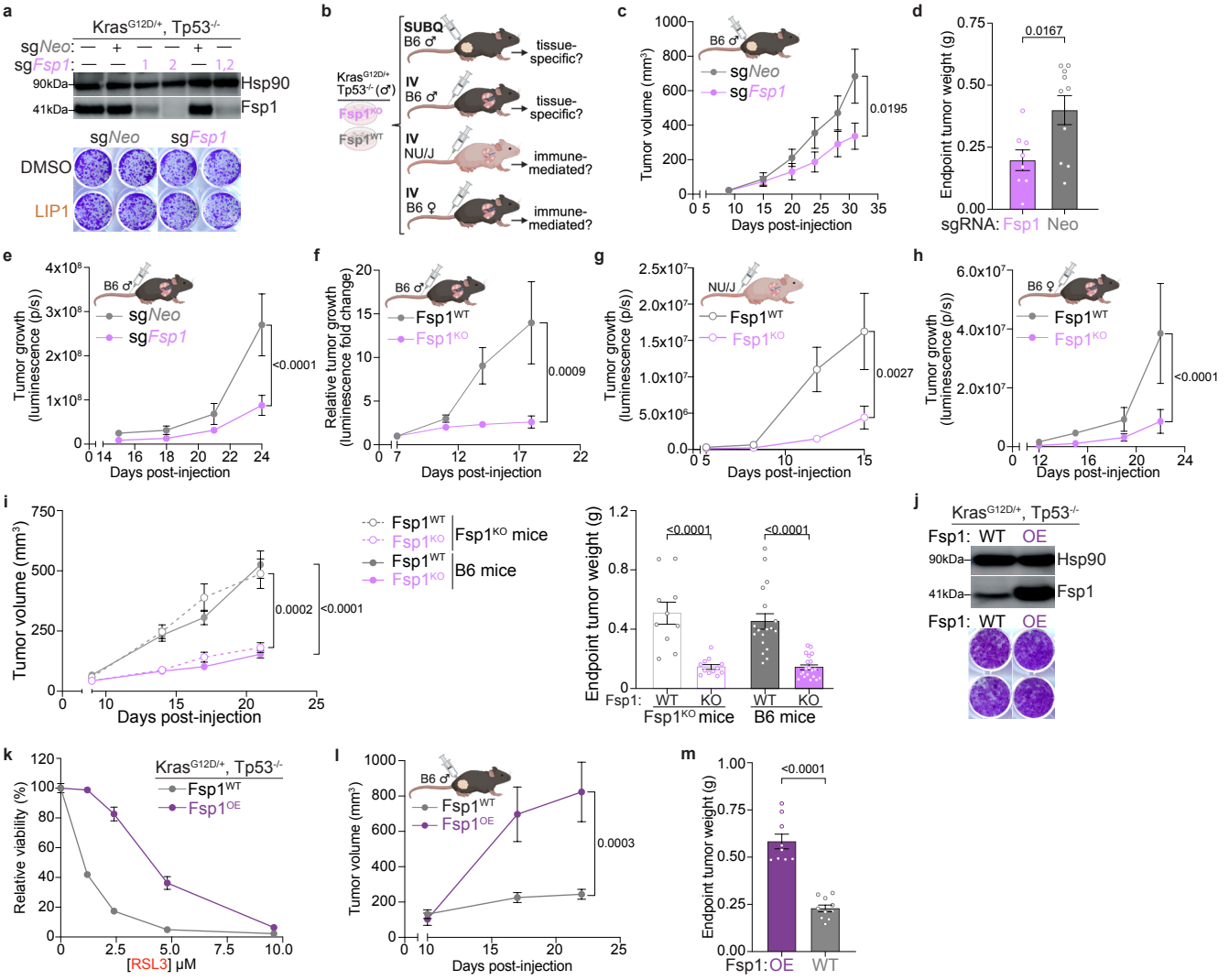

# Extended Data Fig. 5: FSP1 loss *in vitro* does not induce ferroptosis without RSL3

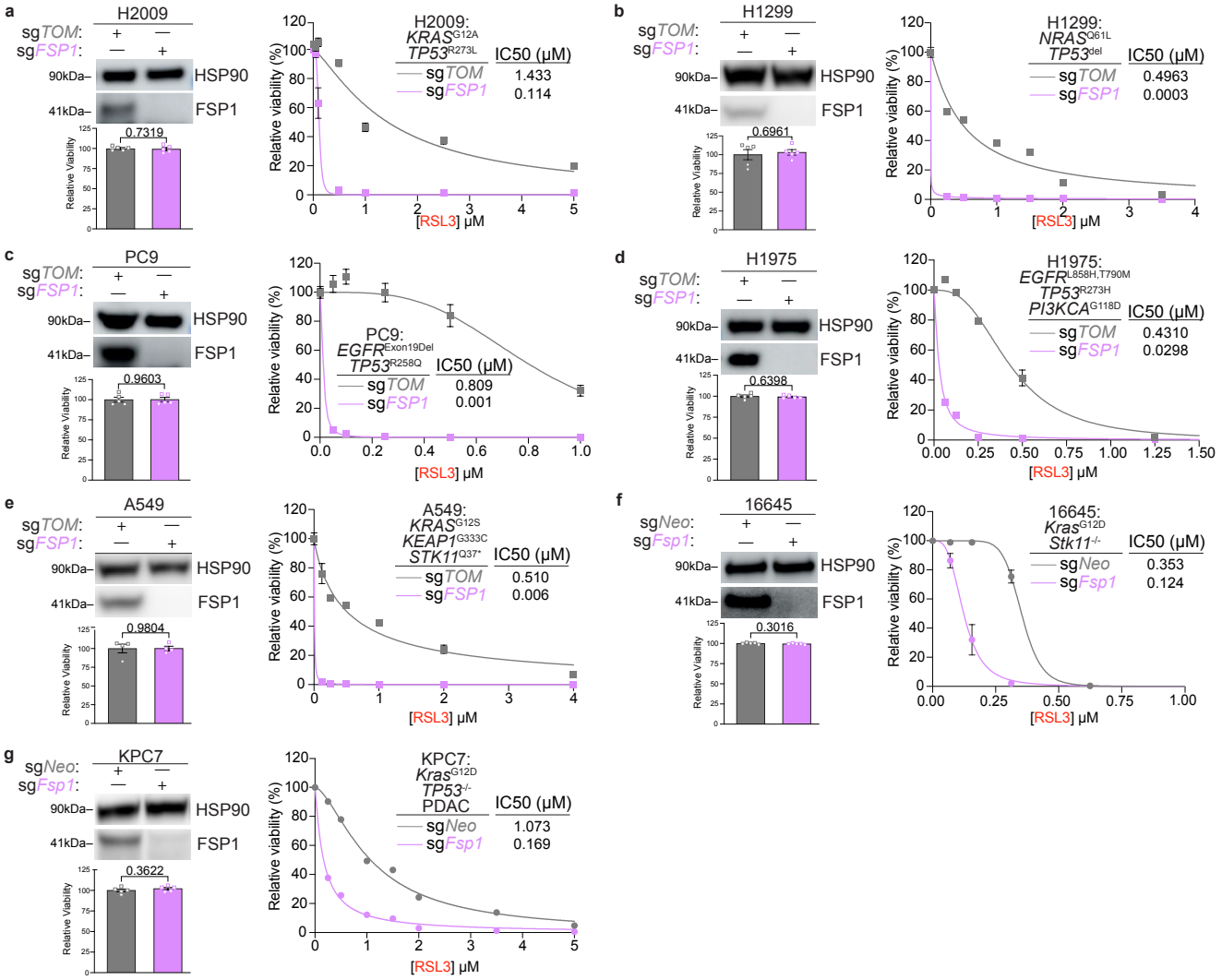

# Extended Data Fig. 6: Fsp1 loss promotes tumor cell ferroptosis

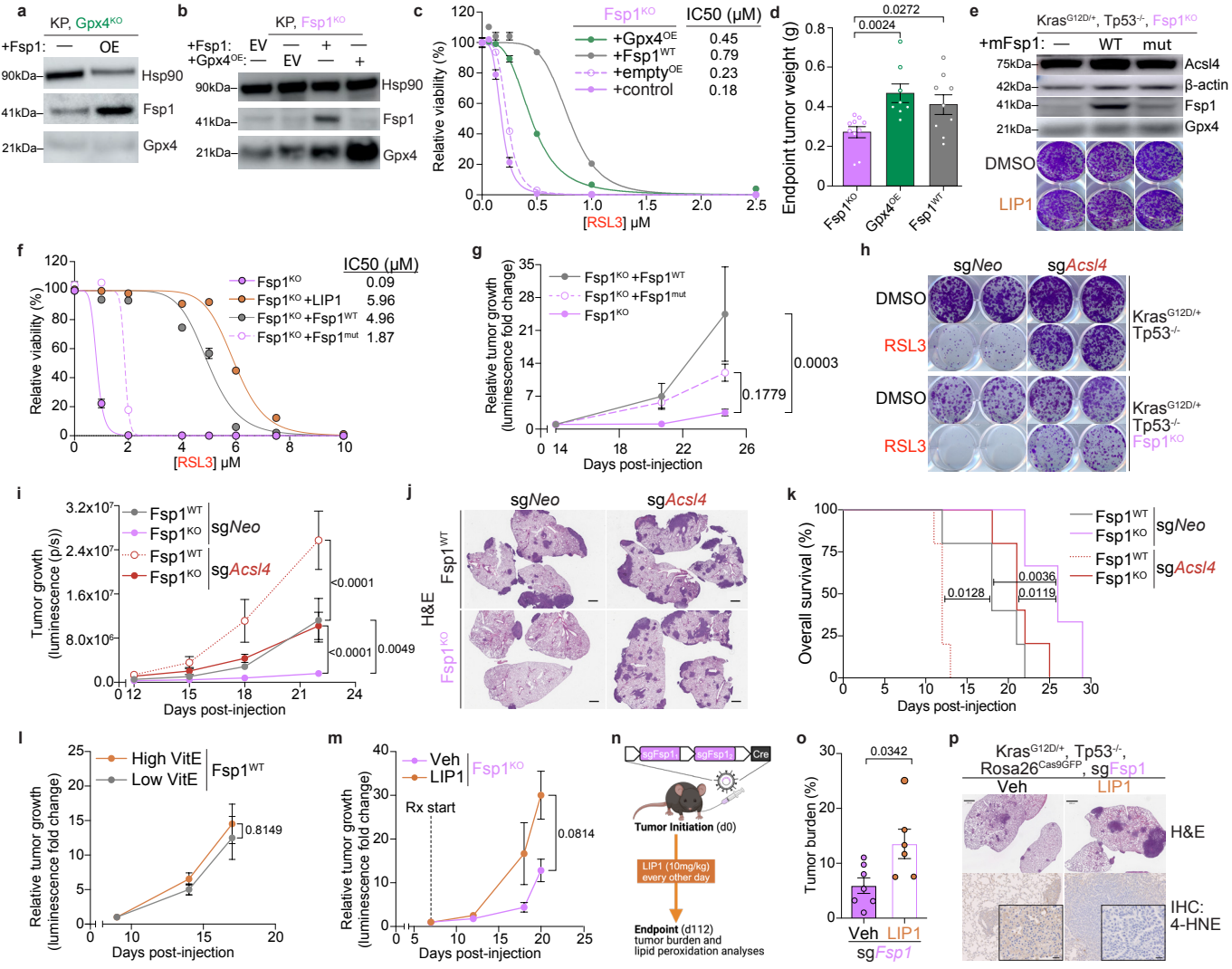

# Extended Data Fig. 7: icFSP1 exerts on-target tumor-suppressive effect

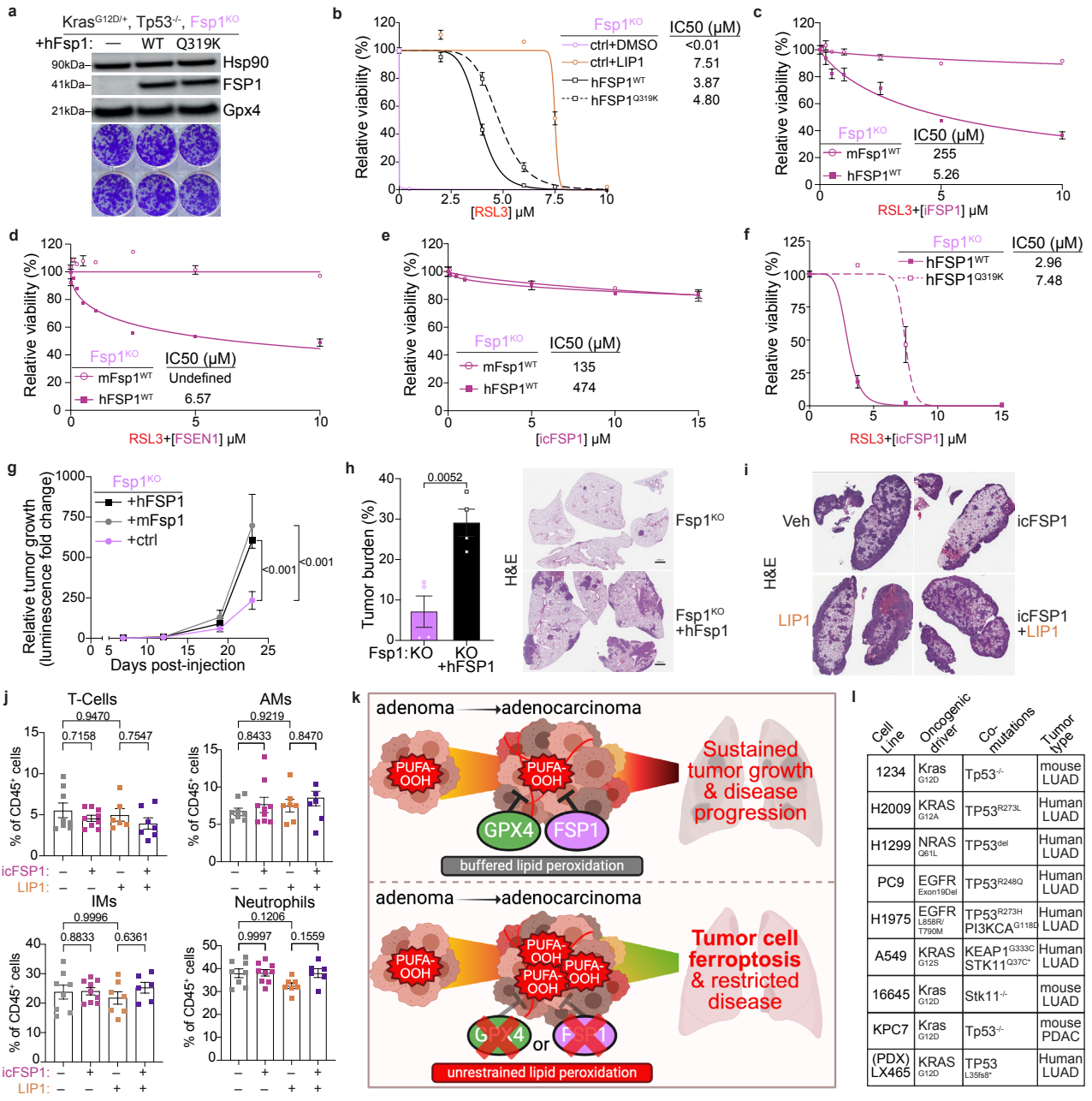


| Cell Line | Oncogenic driver | Co-mutations | Tumor type |
|---|---|---|---|
| 1234 | Kras G12D | Tp53$^{-/-}$ | mouse LUAD |
| H2009 | KRAS G12A | TP53$^{R273L}$ | Human LUAD |
| H1299 | NRAS Q61L | TP53$^{del}$ | Human LUAD |
| PC9 | EGFR Exon19Del | TP53$^{R248Q}$ | Human LUAD |
| H1975 | EGFR L858R/ T790M | TP53$^{R273H}$ PI3KCA$^{G118D}$ | Human LUAD |
| A549 | KRAS G12S | KEAP1$^{G333C}$ STK11$^{Q37C*}$ | Human LUAD |
| 16645 | Kras G12D | Stk11$^{-/-}$ | mouse LUAD |
| KPC7 | Kras G12D | Tp53$^{-/-}$ | mouse PDAC |
| (PDX) LX465 | KRAS G12D | TP53 L35fs8* | Human LUAD |